Acta Materialia 189 (2020) 129–144

Contents lists available at ScienceDirect

Acta Materialia

journal homepage: www.elsevier.com/locate/actamat

Full length article

Critical microstructures and defects in heterostructured materials and their effects on mechanical properties

Yanfang Liu[a], Yang Cao[a,*], Qingzhong Mao[a], Hao Zhou[a], Yonghao Zhao[a], Wei Jiang[a], Ying Liu[b], Jing Tao Wang[b,c], Zesheng You[c], Yuntian Zhu[a,d,**]

[a] Nano and Heterogeneous Materials Center, School of Materials Science and Engineering, Nanjing University of Science and Technology, Nanjing 210094, People's Republic of China
[b] School of Materials Science and Engineering, Nanjing University of Science and Technology, Nanjing 210094, People's Republic of China
[c] Herbert Gleiter Institute of Nanoscience, Nanjing University of Science and Technology, Nanjing 210094, People's Republic of China
[d] Department of Materials Science and Engineering, North Carolina State University, Raleigh, NC 27695, USA

ARTICLE INFO

Article History:
Received 15 October 2019
Revised 22 January 2020
Accepted 2 March 2020
Available online 5 March 2020

Keywords:
Heterostructure
Hetero-deformation induced (HDI) hardening
Back-stress
Shear band
Slip band

ABSTRACT

Systematic study was conducted on the microstructures and mechanical properties of nickel samples with two distinct types of heterostructures. The first is featured with coarse-grained lamellae embedded in a matrix consisting of a very high density of dislocation structures. The second is featured with coarse-grained zones embedded in the ultrafine-grained matrix. The second type of heterostructures exhibits better strength and ductility, although it has a smaller average grain size than the first type. The zone boundaries in the second type of heterostructures are less prone to cracking than those in the first type. Intersecting micro-shear-bands formed net-like patterns in the second type of heterostructures during tensile deformation. This is the first ever observation of structural micro-shear-bands in a heterostructured material. It supports the claim that heterostructure promotes the formation of dispersive shear bands. In contrast, a macroscopic shear band formed and caused early failure of the sample with the first type of heterostructures. Our results indicate that well-developed ultrafine/nano grained matrix in heterostructured materials are necessary for preventing crack formation and shear band localization. This should be considered as a key factor for optimizing the mechanical properties of heterostructured materials.

1. Introduction

Advanced structural materials with outstanding mechanical properties have always been in high demand by industries due to safety, environmental and economical requirements [1,2]. After decades of research and development, the strengths of structural materials have been pushed to a new height by extreme grain refinement to the nanocrystalline regime [3–5]. In conjunction with extreme grain refinement, some deformation mechanisms such as grain rotation, grain boundary sliding and shear banding are likely activated to accommodate applied strains [5–9]. However, diverse deformation mechanisms in nanostructured materials are yet incapable of providing good ductility, because of their limited strain hardening capabilities [10]. Thus, alternative material design strategies are needed to unite the advantages of both coarse-grained (CG) materials and nanostructured materials [11]. Inspired by the composite structures in nature, heterostructured (HS) materials comprising of mixtures of CG zones and nanostructured zones have been developed, and recently received extensive attention from the materials community [12–15].

HS materials in fact cover a broad range of materials [13], including hetero-lamella structured materials [12], gradient structured materials [16–21], laminate structured materials [22,23], dual-phase materials [24–29], harmonic structured materials [30–32], bi-modal structured materials [33–37] and metal matrix composites [38–41]. Their attractive mechanical properties were early understood as the combined effects of the enhanced yield strengths of hard zones and the high strain-hardening capabilities of soft zones [5,11,42], i.e. the popular "rule of mixtures" [41].

In recent years, it has been frequently reported that some HS materials show mechanical properties superior to that predicted by the rule of mixtures [12,17,18,21]. The microstructural architectures of these HS materials share one unifying design principle – the soft zones are constrained by the hard layers or matrices. During plastic deformation of these HS materials, strong back-stress is developed in the soft zones due to the accumulation of geometrically necessary

* Corresponding author.
** Corresponding author at: Nano and Heterogeneous Materials Center, School of Materials Science and Engineering, Nanjing University of Science and Technology, Nanjing 210094, People's Republic of China.
E-mail addresses: y.cao@njust.edu.cn (Y. Cao), ytzhu@ncsu.edu (Y. Zhu).

https://doi.org/10.1016/j.actamat.2020.03.001
1359-6454/

dislocations (GNDs). The back-stress increases the yield strength of the HS materials, meanwhile the strain partitioning during the plastic deformation leads to additional hetero-deformation induced (HDI) hardening that helps with retaining ductility [12,15,17].

Very recently, researchers advanced their knowledge in regarding the hard zones in HS materials. Firstly, it was noticed that the ductility of the less-ductile hard zones can be enhanced by the shear band delocalization effect attributed to the architecture of heterostructure [18,22,43]. Secondly, it was proposed that the back-stress in the soft zone induces the forward-stress in the hard zone, and the interaction between back-stress and forward-stress is not a zero-sum game [15]. The forward-stress promotes plastic deformation in the hard zone (by partitioning higher stress to the hard zone from the global applied stress), but how microstructural evolution responds to the forward-stress is not yet known.

According to Taylor's strain hardening model, statistically stored dislocations (SSDs) and GNDs contribute in the same way to flow stress [10,44,45]. During strain hardening, SSDs are trapped into positions of local energy minima [46] and GNDs accumulate in areas with strong strain misfit/gradient (e.g. interfaces) [13,47]. As a result, various dislocation structures such as dislocation cells and dislocation walls, microbands and slip bands are developed, making critical contributions to the on-going plastic deformation [48,49]. Accordingly, in-depth understanding of the dislocation structures and related issues is critical for studying the strain hardening effect in HS materials, and is a prerequisite for successful development of advanced HS materials with optimized mechanical properties.

Recently, it has been proposed that the formation of dispersive shear bands (shear band delocalization) is a common phenomenon in HS materials [22,43,50,51]. This supposition was drawn from the results that numerous shear bands of much smaller sizes were found in some HS materials, rather than a few macroscopic shear bands that may quickly lead to catastrophic failure of the materials. This supposition is reasonable, but its universality among HS materials still requires further investigation. Based on the dislocation mechanics of shear banding proposed by Armstrong and Zerilli [52] and some published theoretical and experimental work [53–55], the propensity for shear banding varies from material to material due to different intrinsic materials properties. In general, the propensity for shear banding is in a descending order for materials with hexagonal close packed (hcp) structures, face-centered-cubic (fcc) structures and body-centered-cubic (bcc) structures [5,52]. The propensity for shear banding is much higher in materials with low stacking fault energies (SFEs) than the ones with high SFEs [53]. The propensity for shear banding is high in nanostructured materials and low in CG materials [7,9].

Logically, for HS materials consisting of CG soft zones and nanostructured hard zones, shear bands are likely to form in hard zones, meanwhile the confinement by the soft zones is effective in suppressing the expansion of shear bands [18]. This hypothesis is consistent with the concept of shear band delocalization in HS materials [15,22,43]. On the other hand, shear banding is significantly delayed in the deformation process of high SFE materials such as Al and Ni, despite of small grain sizes [9,53]. This is in contrary to large numbers of shear bands observed at comparatively low stain levels in these HS materials [22,43]. Besides, the shear bands observed so far in HS materials are bands of strain concentration rather than actual structural shear bands [22,43,50, 51]. Therefore, it is still necessary to investigate shear band delocalization for in-depth understanding of the mechanical behaviors of HS materials.

In this work, critical microstructures and defects including dislocation structures, shear bands and grains in HS materials are carefully studied. The correlation between microstructural architecture and mechanical properties is investigated in detail. Solid experimental results reveal that the distribution of soft zones is critical for shear band delocalization and dispersion. Certain degree of microstructural difference between hard and soft zones is necessary for enhanced back-stress strengthening and HDI strengthening [15]. The deformation mechanisms for strain accommodations in hard and soft zones, and their connections with HDI stresses are discussed.

2. Experimental procedures

A commercial purity nickel (Ni, 99.3 wt.%) is chosen as the model material in the present work. The as-received material has equiaxed grains with an average size of ~56 μm. Microscopic annealing twins are randomly found. Previous work on such commercially pure Ni, processed through primary grain refinement by equal-channel angular pressing (ECAP), followed by a secondary geometrical refinement via liquid nitrogen rolling (LNR), yields a uniformly nanolaminated structure, with a lamellar boundary spacing of ~ 40 nm, and yield strength of ~ 1.5 GPa with quite limited ductility [56]. In the present work, two processing routes are selected to obtain heterogeneous lamellar structures in Ni. Route 1 is cryogenic rolling followed by annealing treatment. In route 1, a plate sample with a dimension of 60 mm × 50 mm × 10 mm was firstly immersed in liquid nitrogen for 20 min, then the sample was rolled repetitively to a total thickness reduction of ~84%. Each rolling pass caused a thickness reduction of ~2%; The sample was immersed in liquid nitrogen for 5 min right after each rolling pass. The cold rolled sample was annealed, in an electric resistance furnace under vacuum protection, at 500 °C for 13 min to finally obtain the heterogeneous microstructure as shown in Fig. 1a. In route 2, sample bars with a dimension of 10 mm × 10 mm × 70 mm were firstly processed by ECAP with 0.4 mm/s pressing speed at room temperature via Bc route [57] for 8 passes to a total strain of ~8. The ECAP-pressed samples were further processed by the same cryogenic rolling procedures used in route 1 to a total thickness reduction of ~84%. The deformed samples were annealed at 475 °C for 5 min, to finally obtain the heterogeneous microstructure as shown in Fig. 1b. The samples processed through route 1 and route 2 are hereafter referred to as LNR-500 °C-13 min and ECAP+LNR-475 °C-5 min, respectively. The annealing temperatures and time for both model samples were chosen based on a series of annealing tests in which a series of annealing temperatures in the range of 300 °C–500 °C and a series of annealing time in the range of 3 min–60 min were selected. LNR-500 °C-13 min and ECAP+LNR-

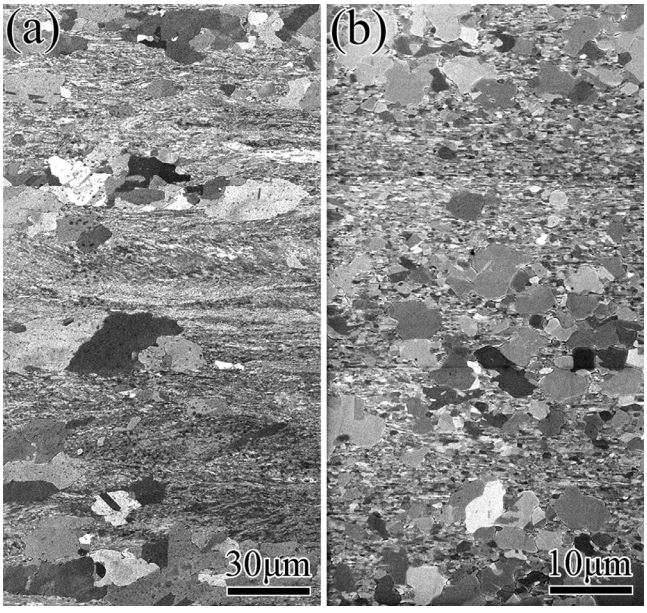

Fig. 1. SEM images showing (a) heterogeneous microstructures in a LNR-500 °C-13 min sample, and (b) heterogeneous microstructures in an ECAP+LNR-475 °C-5 min sample, respectively.

475 °C-5 min are the ones with the best combination of strength and ductility in the corresponding subsets of samples. Mechanical properties of the annealed samples are provided in *Appendix 1 - supplementary materials*. Partial recrystallization by annealing is an effective procedure for processing hetero-structured materials; readers are referred to the reference [12,58] for details.

The as-received sample, LNR-500 °C-13 min and ECAP+LNR-475 °C-5 min samples were cut to a gauge dimension of 10 mm × 2.5 mm × 1.6 mm for uniaxial tensile tests using an LFM-20 kN universal tensile machine at room temperature with a strain rate of $1.6 \times 10^{-3}\,s^{-1}$. Repetitive unloading-reloading tensile tests were conducted at a strain rate of $5 \times 10^{-4}\,s^{-1}$ and a load-controlled unloading rate of 20 N/s to a minimum load of 10 N. A mechanical extensometer was used in all tensile tests.

The microstructures of the sample materials were quantitatively and qualitatively analyzed by scanning electron microscopy (SEM), electron back-scattered diffraction (EBSD), transmission Kikuchi diffraction (TKD) and transmission electron microscopy (TEM). Samples for SEM and EBSD analysis were mechanically polished and subsequently electro-polished with an electrolyte consisting of 12.5% perchloric acid, 37.5% acetic acid and 50% alcohol, under the voltage of ~15 V at room temperature for 30 s. SEM and EBSD analysis were performed using a Zeiss Auriga scanning electron microscope. Samples for TKD and TEM characterization were prepared by firstly grinding and polishing to a thickness of 60 μm, then electropolishing with an electrolyte consisting of 33% nitric acid and 67% methanol, under an operating current of ~60 mA, at a temperature of −40 °C, until a central perforation was observed. TEM was performed with a TECNAI-G2-20-LaB6 microscope operating at 200 kV. (TKD results are provided in *Appendix 2 - supplementary materials*.)

3. Results

3.1. Microstructural evolution of heterostructured Ni during the uniaxial tensile test

Prior to uniaxial tensile tests, the LNR-500 °C-13 min sample has CG lamellae embedded in the matrix consisting of a very high density of dislocation structures such as cell walls and dense dislocation walls [5,48], as shown in Fig. 1a and Fig. 2a. In the CG lamellae, grain boundaries (GBs) are sharp and clear. However, in the matrix GBs and dislocation walls are hardly discriminated by the mixed signal of atomic number contrast and orientation contrast in the SEM image (Fig. 1a). EBSD analysis is very helpful in providing information about both dislocation structures and textures [59]. In Fig. 2a, black lines delineate GBs with misorientation angles above 15°. White lines delineate low angle boundaries in the range of 2°–15°, which are mostly cell walls and dense dislocation walls (DDWs) [60]. High densities of dislocation structures in the matrix significantly increase the strength of materials. Therefore, the matrix is recognized as the hard zone and the CG lamellae are recognized as the soft zones. The volume fractions of the soft (~42.5%) and hard zones (~57.5%) were calculated based on SEM images including the typical one shown in Fig. 1a, by a stereological method. Description of the stereological method is provided in *Appendix 3 - supplementary materials*.

As shown in Fig. 1b, ECAP+LNR-475 °C-5 min samples have CG zones embedded in the ultrafine-grained matrix. As shown in Fig. 2b, GBs delineated by black lines in both CG zones and ultrafine-grained matrix are sharp and clear, indicating that significant recovery and recrystallization have been achieved during heat treatment. Sharp change in color can be seen from grain to grain, indicating weak textures or mixed textures in the material. In this case, the matrix is also recognized as the hard zone and the CG zones are recognized as the soft zones. The volume fractions of the soft zones and hard zone are ~54.6% and ~45.4%, respectively. Although, the ultrafine-grained zone has a slightly smaller volume fraction, it is still recognized as the matrix due to the continuous and interconnected spatial distribution.

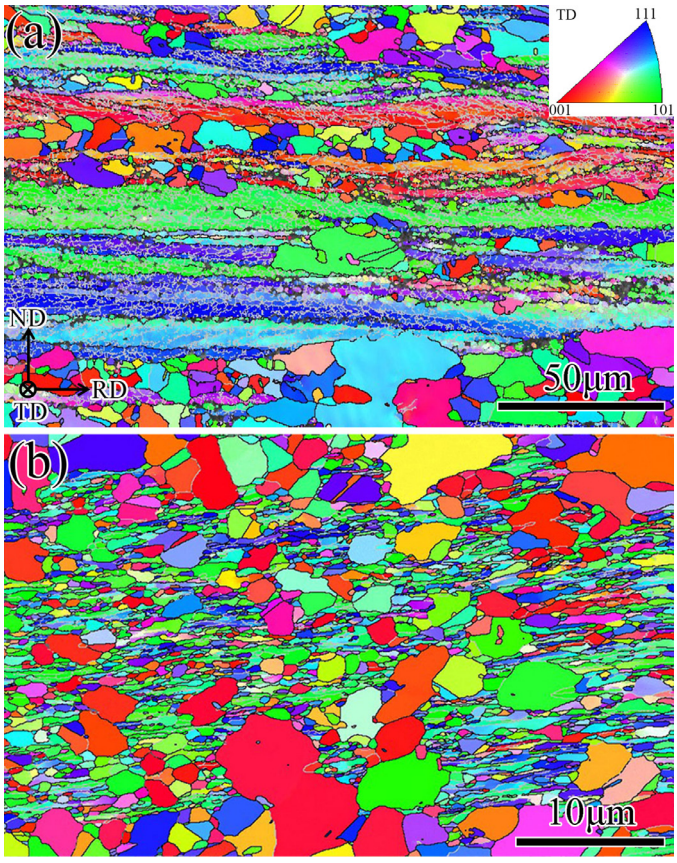

Fig. 2. EBSD images showing heterogeneous microstructures in (a) a LNR-500 °C-13 min sample, and (b) an ECAP+LNR-475 °C-5 min sample. (The color code used for the EBSD images is inserted in (a)).

Fig. 3a shows the ideal orientation distribution functions (ODFs) of possible texture components and fibers in fcc alloys, when the ODF sections are at $\varphi_2 = 0°, 35°, 45°, 60°$ and 65°. The colored symbols correspond to the texture components found in the LNR-500 °C-13 min and ECAP+LNR-475 °C-5 min samples before tensile tests. Fig. 3b shows ODFs of a typical LNR-500 °C-13 min sample before tensile test. By matching Fig. 3b to a, the main textures are determined to be copper, S, brass, R, BR and cube orientations, and the corresponding volume fractions are 18.9%, 17.6%, 12.2%, 9.62%, 9.38% and 3.39%, respectively, in the LNR-500 °C-13 min sample. Copper, S and brass textures are commonly found in fcc materials with high SFEs after cold rolling. R, BR and cube textures are normally formed by recrystallization in fcc materials. The co-existence of a large portion of rolling textures and a small portion of recrystallization textures in the LNR-500 °C-13 min sample indicates that recrystallization occurred during annealing at 500 °C for 13 min.

In contrast, the ECAP+LNR-475 °C-5 min sample has a mixture of copper, S, cube, R, BR and brass textures as shown in Fig. 3c, and the corresponding volume fractions are 17.7%, 15.4%, 14.5%, 9.56%, 4.67% and 3.51%, respectively. Despite of high volume fractions of rolling textures (copper and S textures), a strong cube texture is noticed in the material, indicating that recrystallized grains have been well developed somewhere in the material. Cube texture is the typical recrystallization texture in fcc materials with high SFEs such as Al and Ni. The ECAP+LNR-475 °C-5 min sample have a significantly stronger cube texture than the LNR-500 °C-13 min sample, by comparing Fig. 3a and b. This indicates that recrystallization and recovery could possibly be more pronounced in the ECAP+LNR-475 °C-5 min sample than the LNR-500 °C-13 min sample.

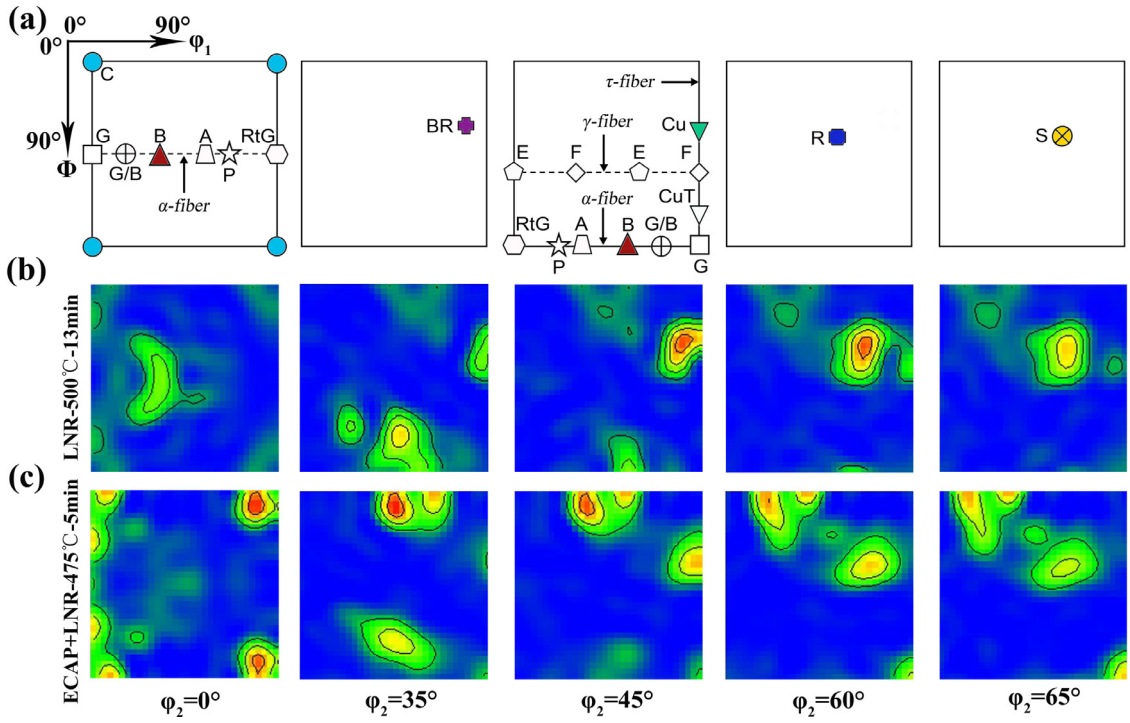

Fig. 3. (a) Schematic illustration of possible texture components and fibers formed in fcc alloys (ODF sections at $\varphi_2 = 0°$, 35°, 45°, 60° and 65°); Textures in (b) a LNR-500 °C-13 min sample and (c) an ECAP+LNR-475 °C-5 min sample, revealed by ODF sections at $\varphi_2 = 0°$, 35°, 45°, 60° and 65° (Texture components: *C* = Cube, *B* = Brass, *G* = Goss, *G*/*B* = Goss/Brass, RtG = Rotated Goss, BR=Brass recrystallization texture, Cu = Copper, CuT = Copper Twin, *A* = *A*-orientation, *E* = *E*-orientation, *F* = *F*-orientation, *P* = *P*-orientation, *R* = *R*-orientation and *S* = *S*-orientation).

In the LNR-500 °C-13 min samples, Fig. 4a shows a clear difference between soft zones and the hard zone in terms of microstructures. One can notice that a few cracks (marked by arrow pairs in Fig. 4a) formed at interfaces between the hard zone and soft zones. The cracks are correlated with locally accumulated dislocations and the GB structures, which will be discussed later. As shown in Fig. 4b, low densities of randomly scattered dislocations are seen in the coarse grains of the soft zones. Along the zone boundary in a soft zone (lower part of Fig. 4b), there are some residual dislocations and the associated fan-shaped strain contours. Hence, strain gradients at the interfaces are already present prior to the tensile test. As shown in Fig. 4c, in the hard zone typical deformation-induced boundaries such as cell walls, DDWs and micro-bands [5,60] subdivided the elongated coarse grains into countless ultrafine dislocation cells [47]. In the inserted selected area diffraction (SAD) pattern, the diffraction spots are extended to arcs of a few degrees, indicating that the deformation-induced boundaries are low angle boundaries. The differences in microstructures of the soft and hard zones in the LNR-500 °C-13 min sample are also evidenced by the clear difference of the densities of low angle boundaries shown in Fig. S2a in *Appendix 2 - supplementary materials*. These deformation-induced boundaries can effectively contribute to Hall–Petch type boundary strengthening [60]. Therefore, the flow stress of the hard zone should be higher than the soft zones.

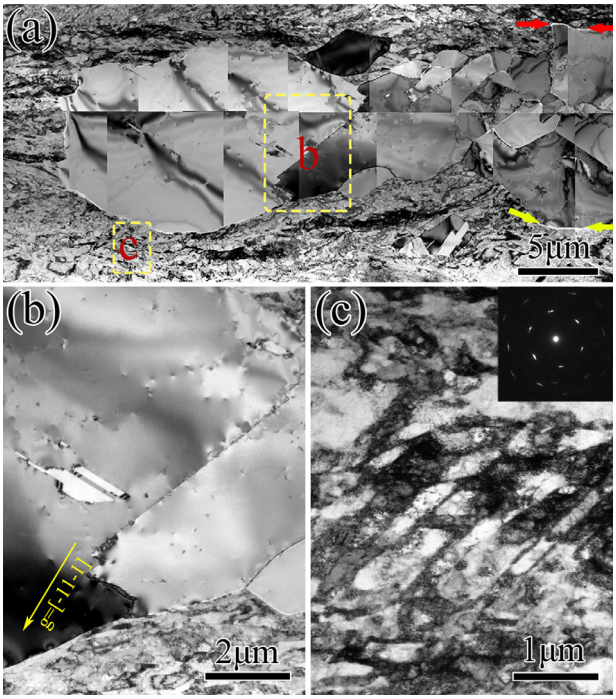

Fig. 4. (a) A low magnification TEM image showing typical microstructures in a LNR-500 °C-13 min sample before tensile test (some cracks along zone boundaries are marked by arrow pairs); (b) A magnified TEM image of the area marked "b" in (a); (c) A magnified TEM image of the area marked "c" in (a), and the corresponding SAD pattern.

In the ECAP+LNR-475 °C-5 min sample, Fig. 5a shows that dislocation densities in CG zones are very low. A magnified image of a typical coarse grain shown in Fig. 5b reveals that dislocation densities are also low adjacent to zone boundaries. This is understandable that despite of the significant difference in flow stresses between soft and hard zones, the samples are still single-phased materials. Thus, without any difference in Young's modulus and lattice structure [5], considerable amounts of GNDs can be recovered with sufficient recrystallization. Fig. 5c illustrates the well-developed ultrafine grains in the hard zones. The ultrafine grains are elongated along the rolling direction. Interconnecting boundaries or dislocation walls are observed in these elongated grains [5,60]. Scattered diffraction spots shown in the inset also verify that these are elongated grains rather than dislocation structures.

At the strain of ~0.02, both soft and hard zones in LNR-500 °C-13 min samples have plastically deformed, evidenced by the

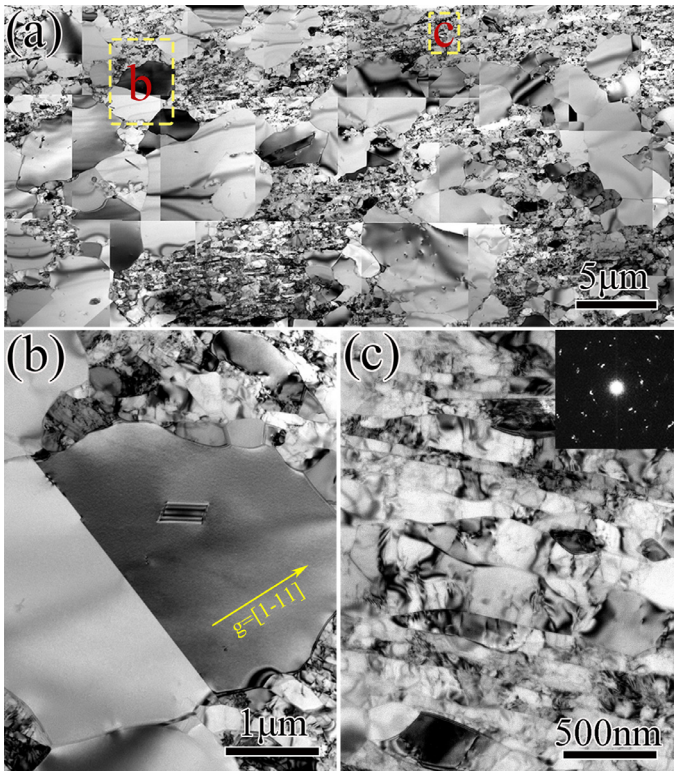

Fig. 5. (a) A low magnification TEM image showing typical microstructures in an ECAP +LNR-475 °C-5 min sample before tensile test; (b) A magnified TEM image of the area marked "b" in (a); (c) A magnified TEM image of the area marked "c" in (a), and the corresponding SAD pattern.

significant increase in dislocation densities as shown in Fig. 6a. A large amount of dislocations tangled together at the interior of coarse grains, as shown in Fig. 6b. Again, some cracks (marked by arrow pairs in Fig. 6a and b) are found at interfaces between the hard zone and soft zones. The cracks might be caused by the high densities of dislocations (high stress concentrations) at the interfaces. Once the material is thinned by electro-polishing to a thickness of a few tens of nanometers, three-dimensional constraint on interfaces may be removed. Then some highly strained interfaces begin to crack and relieve stress. In contrast, a twin boundary (Fig. 6c) inside a soft zone has also blocked a large amount of dislocations, but the twin boundary has not cracked. Provided that the energy state of a twin boundary is significantly lower than an ordinary GB [61], the twin boundary was still intact in this thin sample while neighboring GBs had begun to crack. In the hard zone shown in Fig. 6d, DDWs and micro-bands have sharpened due to mutual annihilation of dislocations at the boundaries as a part of tensile plastic deformation [48,60]. However, the interiors of the hard zones were still populated by extended dislocation boundaries of low angles rather than subgrain boundaries, as revealed by the inserted SAD pattern.

At the same strain of ~0.02, the ECAP+LNR-475 °C-5 min samples have also deformed by dislocation slip, as shown in Fig. 7a. Dislocation entanglement and cell formation were found in the coarse grains as revealed by Fig. 7b. Different from the LNR-500 °C-13 min sample, cracks were not found in the ECAP+LNR-475 °C-5 min TEM samples. Therefore, a high density of dislocations can be seen at the interface between soft and hard zones, as shown in Fig. 7b. From the TEM image of Fig. 7c, it can be seen that some ultrafine grains are rich of dislocations, but the size of the grains are not much different from the ones in Fig. 5c. Thus, dislocation slip was still the dominant deformation mechanism in the ultrafine-grained zones.

Both LNR-500 °C-13 min and ECAP+LNR-475 °C-5 min samples were pulled to the strain levels when necking was apparent. TEM specimens were then taken at the region of necking. Fig. 8a shows the microstructures at the necking region of a LNR-500 °C-13 min sample. A large number of cell blocks, and dislocation cells have formed in the original CG zones. The densities of dislocation structures in both soft and hard zones are so high that it is difficult to distinguish the types of zones at low magnifications. Therefore, TEM images are magnified in order to discriminate soft and hard zones in the sample. As shown in Fig. 8b, dislocation cells are mostly equiaxed with an average size of ~530 nm and cell walls are thick and diffused. In contrast, the dislocation density in the hard zone is still much higher than that in the soft zones, and dislocation cells are elongated, as shown in Fig. 8c.

The microstructures of the soft zones in ECAP+LNR-475 °C-5 min samples at necking are very similar to that of LNR-500 °C-13 min samples as shown in Fig. 9a. and b. The average size of the dislocation cells in the soft zones of ECAP+LNR-475 °C-5 min samples is ~510 nm. The ultrafine grains are still elongated and filled with dislocations, as shown in Fig. 9c. It is important to mention that cracks were still hardly found in the TEM sample, even though the bulk ECAP+LNR-475 °C-5 min samples were pulled to apparent necking.

3.2. Fracture mechanisms in heterostructured Ni

Fractographic analysis by SEM was conducted to reveal the fracture mechanisms and their effects on ductility. Fig. 10a shows the surface morphology of the fracture tip on the transverse plane of a LNR-500 °C-13 min sample. There are two important types of deformation structures – a macroscopic shear band (Fig. 10b) and a massive amount of slip bands (Fig. 10c). The macroscopic shear band has a length of ~350 μm and is directly connected to the fracture surface. The characteristics of the macroscopic shear band (Fig. 10b) match well with the conventional adiabatic shear bands which are commonly found in metallic materials deformed at high strain rates [55] or at the final stage of necking [9,52]. Adjacent to and even on the fracture surface, slip bands are everywhere, as shown in Fig. 10c. The yellow dash lines outline a set of slip bands with similar orientations. Each set of slip bands is strictly confined in a single grain of micrometer size. Knowing that slip bands formed when dislocations slipped to the material's surface [49,62,63], dislocation slip obviously dominated the deformation process until fracture.

The fracture mechanism of the ECAP+LNR-475 °C-5 min samples are different from the LNR-500 °C-13 min samples, as revealed by the surface morphology shown in Fig. 11. The most salient feature in Fig. 11a is the intercrossed micro-ditches all over the area of necking. It can be noticed from Fig. 11b that many of the micro-ditches seem to be in parallel and having an angle of ~ 28.2° (the angle varies in the range of 46.1°–20.7°) to the RD (tensile axis) of the sample. These are also many micro-ditches having much larger angles to the RD. For example, a high angle micro-ditch is inclined to a low angle micro-ditch with an angle of 43.2° that add up to a total angle of 71.4° to the RD. Fig. 11c is a SEM image showing a pair of intercrossed micro-ditches at a high magnification.

The micro-ditches are actually developed from discontinuous micro-shear-bands, which have also been observed in another work [9]. The thin micro-shear-bands sheared across ultrafine grains (an example is marked by a pair of blue arrows) but stopped at the boundaries of coarse grains (marked by a pair of red arrows). Meanwhile, the coarse grains were still deforming by dislocation slip, evidenced by the slip bands in the outlined grain. The spacing between CG lamellae is only about ~10 μm (Figs. 1b and 2b), therefore the lengths of these thin micro-shear-bands are limited to a few or a few tens micrometers. There are thick and deep micro-ditches, which are precursors of micro cracks. According to Fig. 11c, the initiation sites of the cracks are at junctions (marked by red arrows) where micro-shear-bands meet the boundaries of coarse grains. Eventually, many of the

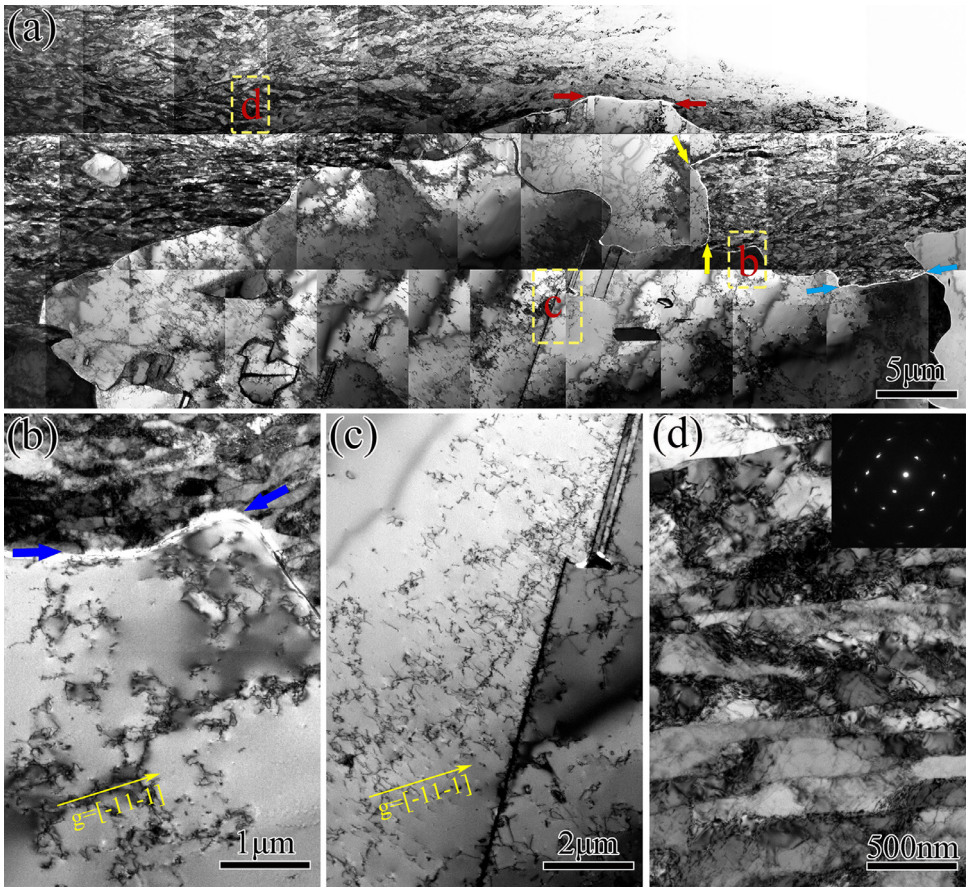

Fig. 6. (a) A low magnification TEM image showing typical microstructures in a LNR-500 °C-13 min sample at an engineering strain of ~0.02 (some cracks along zone boundaries are marked by arrow pairs); (b) A magnified TEM image of the area marked "b" in (a); (c) A magnified TEM image of the area marked "c" in (a); (d) A magnified TEM image of the area marked "d" in (a), and the corresponding SAD pattern.

deep micro-ditches and cracks merge to form large cracks, which lead to failure of the material. Thus, instead of a few large macroscopic shear bands, step-like features and micro-ditches were left on the fracture tip shown in Fig. 11a.

3.3. Mechanical properties of heterostructured Ni

Although the strength–ductility trade-off dilemma has not been broken by introducing heterostructures to Ni, as shown by the

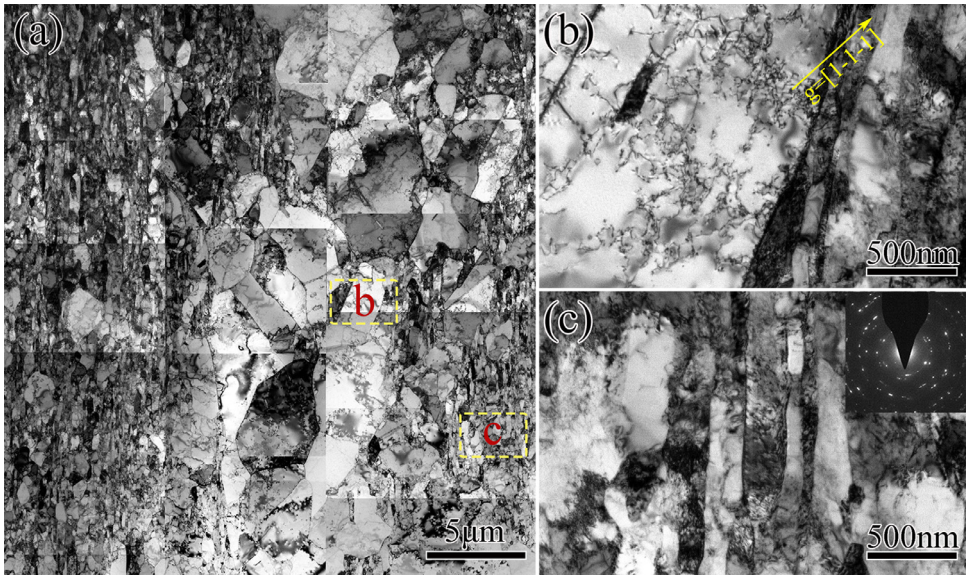

Fig. 7. (a) A low magnification TEM image showing typical microstructures in an ECAP+LNR-475 °C-5 min sample at an engineering strain of ~0.02; (b) A magnified TEM image of the area marked "b" in (a); (c) A magnified TEM image of the area marked "c" in (a), and the corresponding SAD pattern.

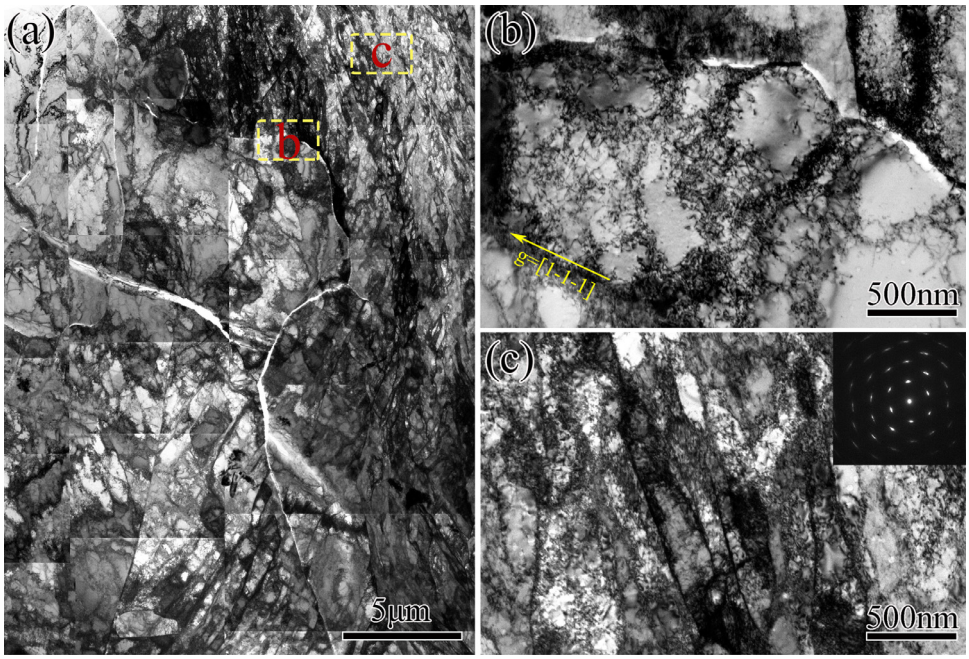

Fig. 8. (a) A low magnification TEM image showing typical microstructures in a LNR-500 °C-13 min sample at necking; (b) A magnified TEM image of the area marked "b" in (a); (c) A magnified TEM image of the area marked "c" in (a), and the corresponding SAD pattern.

engineering stress–strain curves in Fig. 12a. The improvement in mechanical properties by modifying the heterostructures is encouraging. Both ECAP+LNR-475 °C-5 min and LNR-500 °C-13 min samples have significantly better yield strength (YS) and ultimate tensile strength (UTS) than the homogeneous CG sample. The uniform elongations of ECAP+LNR-475 °C-5 min and LNR-500 °C-13 min samples are 12% and 11%, respectively. Correspondingly, the strain hardening parameters (n) of the ECAP+LNR-475 °C-5 min and LNR-500 °C-13 min samples are 0.104 and 0.096, respectively. The strain hardening capabilities of HS materials are lower than the CG material (n = 0.324). Increased volume fractions of ultrafine grains or ultrafine cells in the HS materials, suppress further dislocation generation and slip, and increase the chance for dislocation annihilation at boundaries by thermally activated cross slip and climb [10,33]. As a result, the strain hardening capabilities/parameters of HS materials are lowered, leading to lowered ductility.

Fig. 12b shows typical true stress–strain curves of three different Ni samples obtained by loading–unloading tests. All the unloading–reloading cycles revealed detectable hysteresis with reverse plastic flow even when the overall stress was still in tension. The unloading–reloading hysteresis loops indicate the existence of inhomogeneous deformation in the material. Even in materials with homogeneous CG structures (e.g. black unloading–reloading cycles in Fig. 12b and c), the plastic deformation is still inhomogeneous at microscale, because of the presence of GBs and textures [5,49,52]. Deformation in the near GB regions activates GNDs of multiple slip

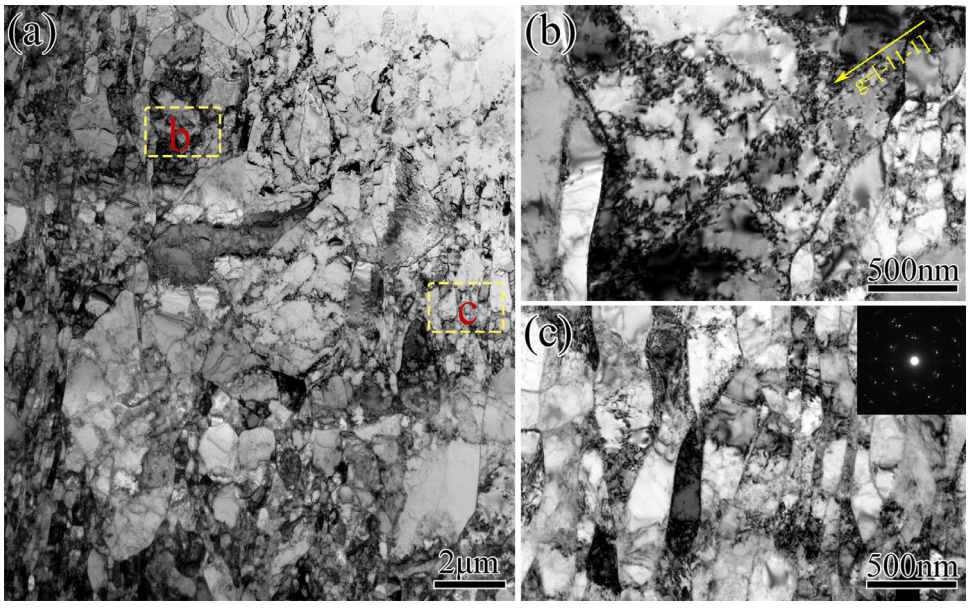

Fig. 9. (a) A low magnification TEM image showing typical microstructures in an ECAP+LNR-475 °C-5 min sample at necking; (b) A magnified TEM image of the area marked "b" in (a); (c) A magnified TEM image of the area marked "c" in (a), and the corresponding SAD pattern.

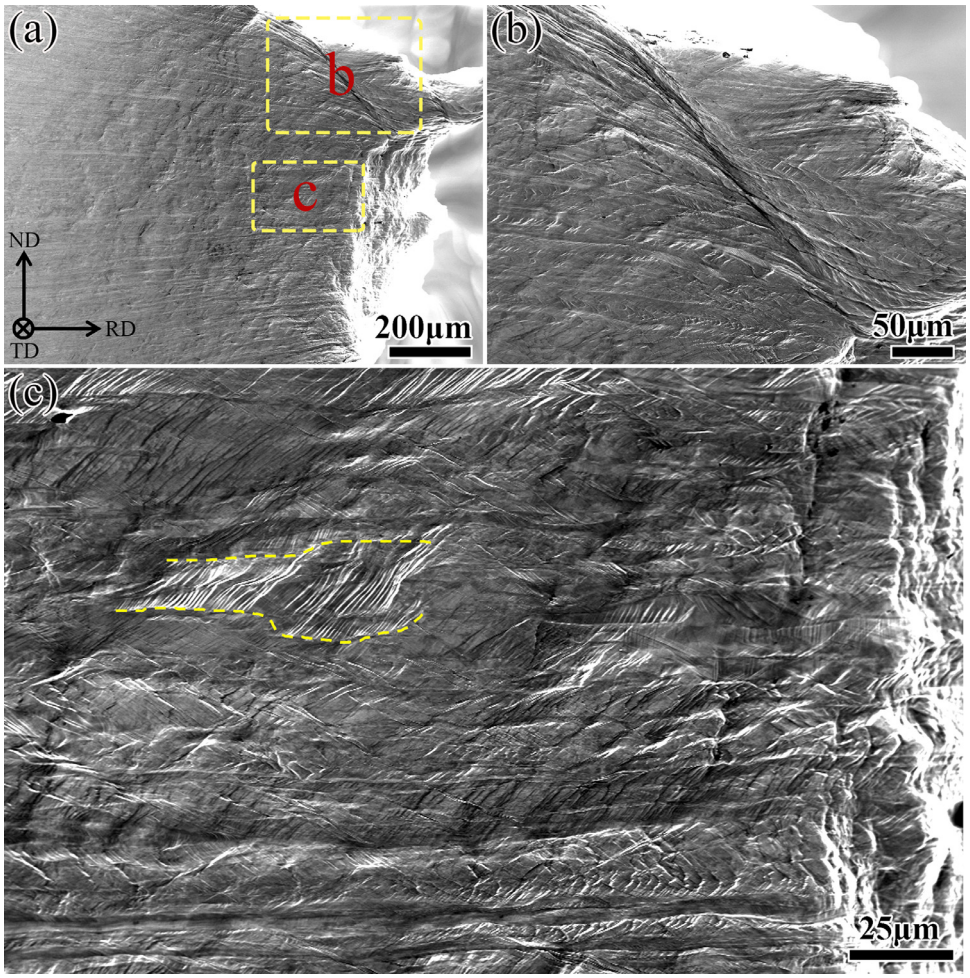

Fig. 10. (a) A low magnification SEM image showing the surface morphology on the transverse plane of a LNR-500 °C-13 min sample at fracture; (b) A SEM image showing a large shear band at the area marked "b" in (a); (c) A magnified SEM image of the area marked "c" in (a).

systems and produces orientation gradients in terms of lattice rotation [44,46,47]. Accumulation of GNDs near GBs produces HDI stresses (formerly known as back-stresses) that cause stress–strain hysteresis during unloading–reloading [15]. According to literatures [64,65], the HDI stress (σ_{HDI}) can be calculated by the equation:

$$\sigma_{HDI} = \frac{\sigma_r + \sigma_u}{2} \quad (1)$$

where the reloading yield stress σ_r and unloading yield stress σ_u can be measured from each hysteresis loop, as exemplified in Fig. 12c. σ_u is taken at the unloading yielding point where the unloading stress-strain curve begins to change from a linear line into a nonlinear curve with the decreasing stress. The slope of the linear (elastic) part of the unloading curve is called the effective unloading Young's modulus, E_u [64]. The accuracies of σ_u and E_u are sensitive to measuring method and human errors. Therefore, the measured values of E_u were compared to the modulus of elasticity of the stress-strain curve. It was found that for ECAP+LNR-475 °C-5 min, LNR-500 °C-13 min and CG Ni samples, the E_u is approximately ~10% (5%–15%) slope reduction from the modulus of elasticity of the sample material. Thus, our measurements of σ_u and E_u have a good consistency, and the measured values have a good accuracy. σ_r is taken at the reloading yielding point where the reloading stress-strain curve begins to deviate from the effective reloading Young's modulus, E_r, under the assumption that $E_r = E_u$. It is worth to mention that Eq. (1) is less sensitive to the errors of measured σ_u and σ_r, in comparison with other proposed equations [64]. Therefore, the HDI stresses calculated in this work are reliable.

The variations of HDI stress as a function of strain are provided in Fig. 12d. At all measured strain levels, the HDI stresses in ECAP+LNR-475 °C-5 min and LNR-500 °C-13 min samples are significantly higher than the CG sample by more than 190 MPa. The HDI stresses in ECAP +LNR-475 °C-5 min, LNR-500 °C-13 min and CG samples increased from 396.5 MPa to 437.6 MPa, 323.9 MPa to 379.6 MPa and 124.8 MPa to 187.9 MPa within the strain range of 0.02 – 0.1, respectively.

4. Analysis

4.1. Statistical analysis

In the soft zones of LNR-500 °C-13 min samples, dislocation densities were low, and GBs were sharp and clear prior to tensile tests, as shown in Figs. 2a and 4a. The grain sizes were in the range of 4–30 μm and averaged at 12.3 μm, according to the statistical analysis of EBSD data and TEM images, as displayed in Fig. 13a. The hard zone was filled with a high density of dislocation boundaries, as shown in Fig. 4c. The high-angle dislocation boundaries are effective in blocking dislocation slip and thus contributing to Hall-Petch strengthening effect in the material [5,60]. Therefore, for the purpose of stress analysis, the transverse and longitudinal boundary spacing of the well-developed dislocation cells were displayed in Fig. 13b and c, respectively. The transverse boundary spacing was in the range of 0.10–0.54 μm and averaged at 0.26 μm. The longitudinal boundary spacing was in the range of 0.24–1.19 μm and averaged at 0.65 μm.

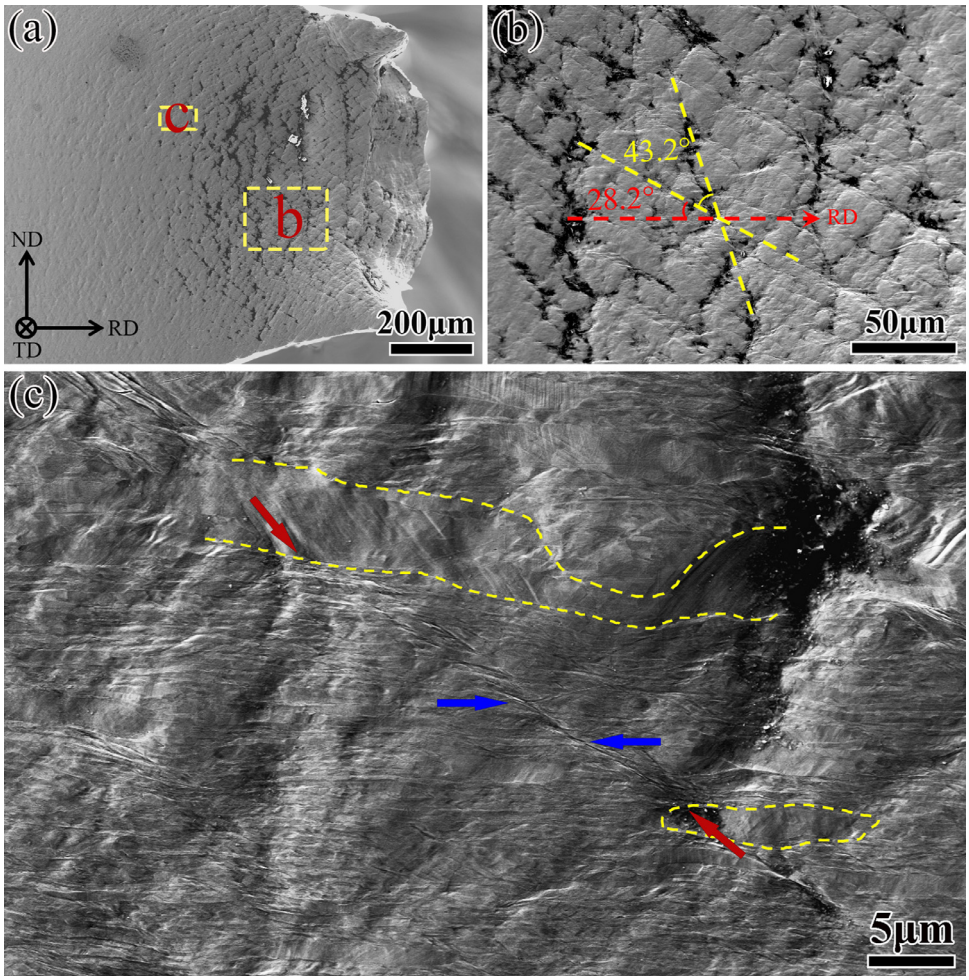

Fig. 11. (a) A low magnification SEM image showing typical surface morphology on the transverse plane of an ECAP+LNR-475 °C-5 min sample at fracture; (b) and (c) are magnified SEM images of the areas marked "b" and "c" in (a), respectively.

When a LNR-500 °C-13 min sample was pulled to necking at a tensile elongation above 11%, significant amounts of dislocation structures were formed in the soft zones as shown in Fig. 8b. The dislocation cells in the soft zones were mostly equiaxed with an average cell size of 0.53 μm as shown in Fig. 13d. In the hard zone, the transverse boundary spacing was further reduced to an average of 0.18 μm, but unexpectedly the longitudinal boundary spacing was slightly increased to an average of 0.82 μm.

In order to clarify if structure refinement occurred in the hard zone of the LNR-500 °C-13 min sample, the equivalent boundary spacing (D_{av}^{eqv}) in the hard zones before and after the tensile test shall be assessed [60,66].

For transverse boundaries, the average boundary area per unit volume is related to the average transverse boundary spacing (D^{trans}) as:

$$S_V^{trans} = \frac{1}{D^{trans}} \tag{2}$$

For longitudinal boundaries, the average boundary area per unit volume is related to the average longitudinal boundary spacing (D^{long}) as:

$$S_V^{long} = \frac{\pi}{2D^{long}} \tag{3}$$

The equivalent boundary area per unit volume (S_V) is:

$$S_V = S_V^{trans} + S_V^{long} \tag{4}$$

Then, the equivalent boundary spacing in the hard zone can be estimated as:

$$D_{av}^{eqv} = \frac{2}{S_V} \tag{5}$$

In this work, $D^{trans} = 0.26$ μm and $D^{long} = 0.65$ μm are obtained from the statistical data in Fig. 13b and c, respectively. By performing calculations with Eqs. (2)–(5), the equivalent boundary spacing in the hard zone before tensile test is estimated to be 0.32 μm. By performing the same calculation procedure for the hard zone at necking, the equivalent boundary spacing is estimated to be 0.27 μm. Thus, moderate refinement in dislocation structures occurred in the hard zone of the LNR-500 °C-13 min sample during tensile deformation, in despite of a slight increase in the longitudinal boundary spacing.

The grains in the ECAP+LNR-475 °C-5 min samples are smaller than that of the LNR-500 °C-13 min samples as revealed by the statistical data in Fig. 14. The grain sizes in the soft zones are in the range of 0.9–6.4 μm, and averaged at 2.4 μm, as displayed in Fig. 14a. The hard zone of the ECAP+LNR-475 °C-5 min sample consists of elongated ultrafine grains aligned nearly parallel to the loading direction as shown in Figs. 1b and 2b. The transverse grain sizes (lamellar GB-spacing) in the ECAP+LNR-475 °C-5 min sample were in the range of 0.05–0.49 μm and averaged at 0.19 μm (Fig. 14b). The longitudinal boundary spacing (interconnecting boundaries [5,60] and GBs) was in the range of 0.18–1.26 μm and averaged at 0.66 μm (Fig. 14c). Therefore, the equivalent boundary spacing was calculated to be

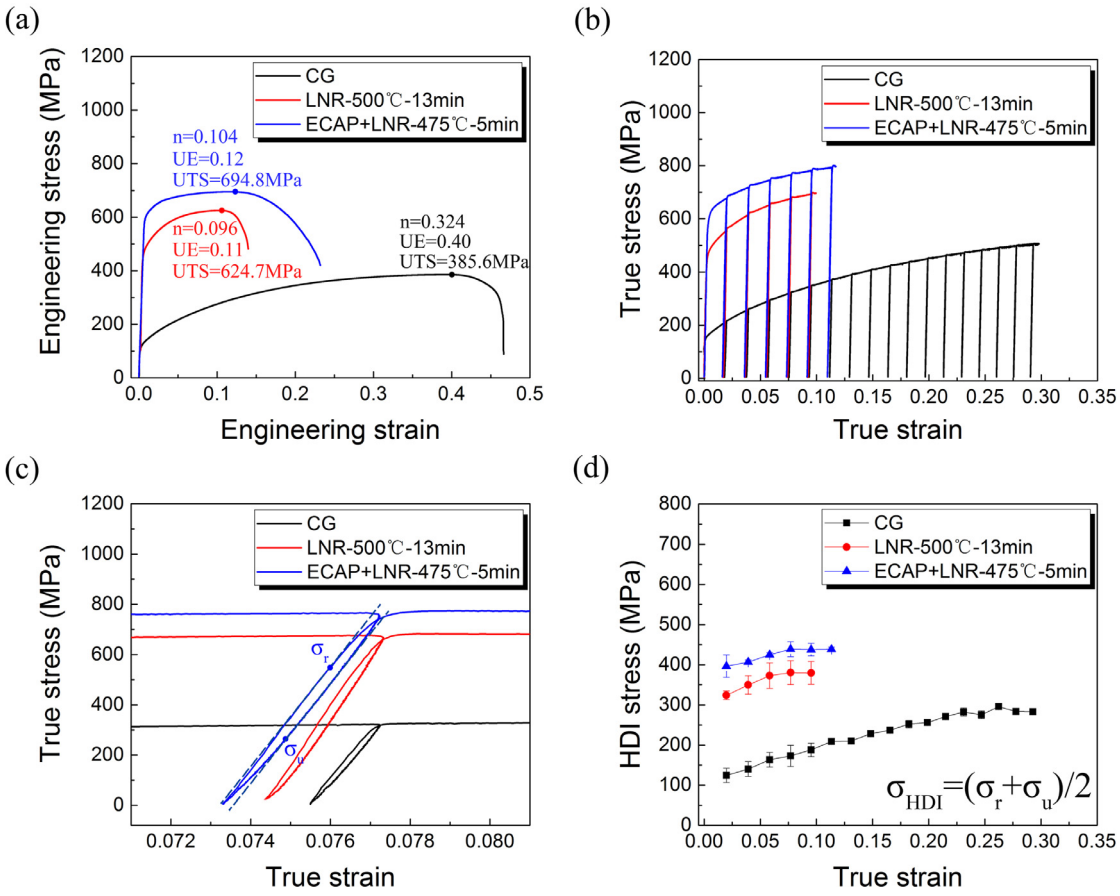

Fig. 12. (a) Engineering stress–strain curves of as-received coarse-grained sample, LNR-500 °C-13 min sample and ECAP+LNR-475 °C-5 min sample; (b) True stress–strain curves obtained by loading–unloading (solid) tensile tests; (c) magnified unloading–reloading hysteresis loops taken from a part of (b); (d) HDI stresses derived from the unloading–reloading hysteresis loops in (b).

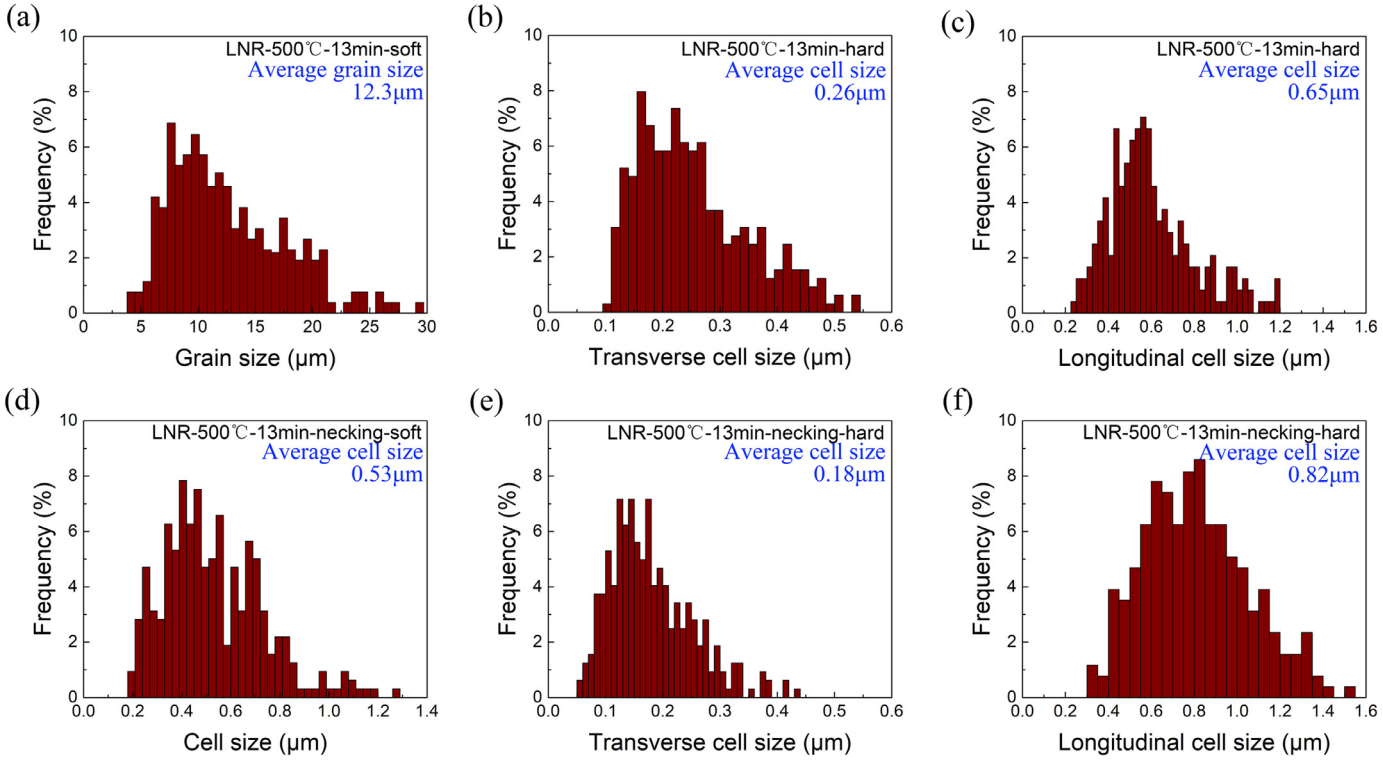

Fig. 13. Charts showing (a) grain size distribution in soft zones, (b) transverse cell size distribution in the hard zone, and (c) longitudinal cell size distribution in the hard zone, in the LNR-500 °C-13 min sample prior to tensile tests. Charts showing (d) cell size distribution in soft zones, (e) transverse cell size distribution in the hard zone, and (f) longitudinal cell size distribution in the hard zone, at the onset of necking in the LNR-500 °C-13 min sample.

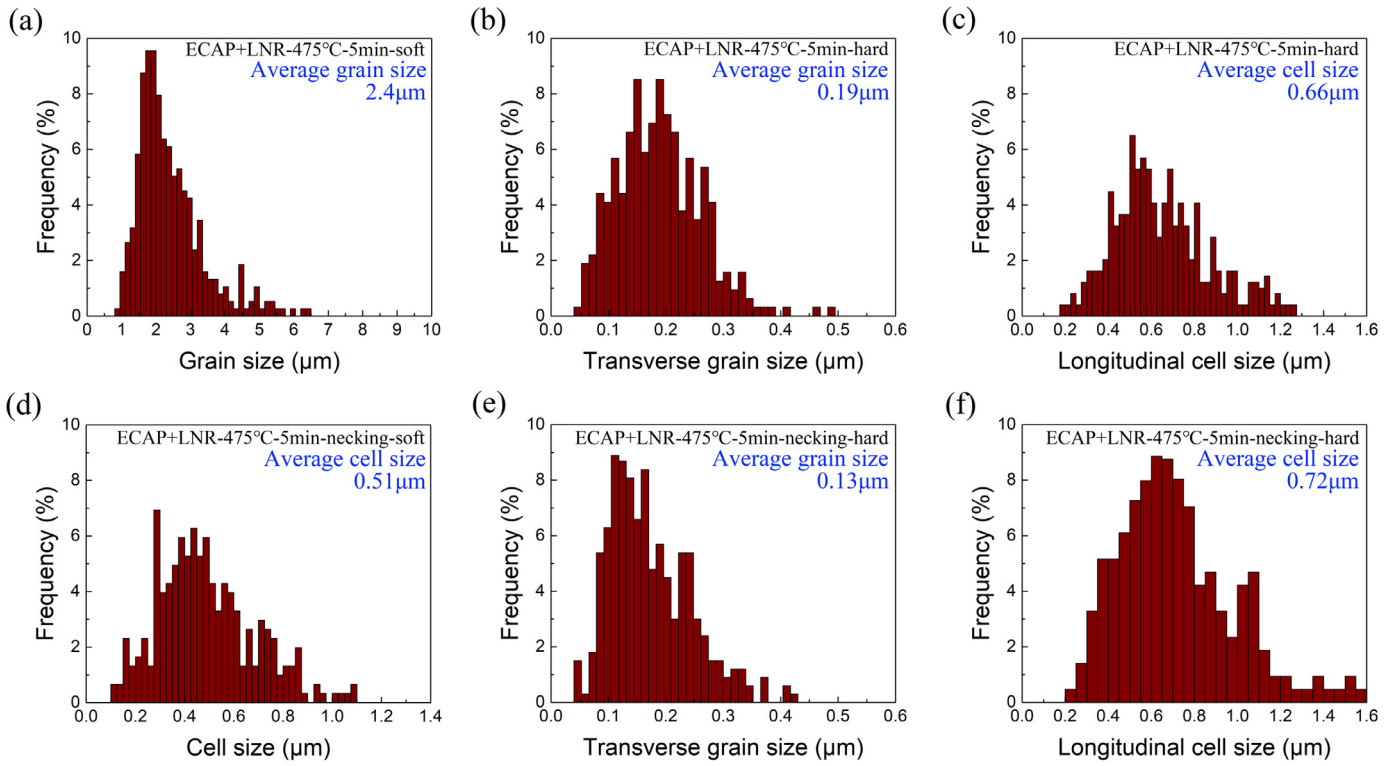

Fig. 14. Charts showing (a) grain size distribution in soft zones, (b) transverse grain size distribution in the hard zone, and (c) longitudinal cell size distribution in the hard zone in the ECAP+LNR-475 °C-5 min sample prior to tensile tests. Charts showing (d) cell size distribution in soft zones, (e) transverse grain size distribution, and (f) longitudinal cell size distribution in the hard zone, at the onset of necking in the ECAP+LNR-475 °C-5 min sample.

0.26 μm. When the sample was pulled to necking at a tensile elongation above 12%, equiaxed dislocation cells with an average size of 0.51 μm formed in the soft zones (Fig. 14d). Interestingly, the average transverse grain size was slightly reduced to 0.13 μm (Fig. 14e) and the average longitudinal boundary spacing was increased to 0.72 μm (Fig. 14f), leading to an equivalent boundary spacing of 0.2 μm, in the hard zone. Grain refinement in the hard zone was unexpected, because grain refinement by deformation induced dislocation structures requires much higher strain than that imposed by the uniaxial tensile test [5]. Considering the global strain is low in a uniaxial tensile test, there should be another grain refinement mechanism in operation. As shown in Fig. 11, discontinuous micro-shear-bands were all over the surface of the necking region. As shown in Fig. 11c, the grains which have been sheared by a shear band, were stretched and tilted along the shear direction. There have been many reports showing that shear banding is effective in grain refinement at local regions [46,55]. Thus, a large amount of shear bands as shown in Fig. 11a are capable of causing the overall grain refinement.

4.2. Structural parameters and strength calculations

The strengths of polycrystalline single-phase materials are governed by both boundary strengthening effect and strain hardening effect [5]. It is a common practice to predict the boundary strengthening effect by employing the empirical Hall–Petch equation [66]:

$$\sigma_d = \sigma_0 + K_{HP} D_{av}^{-1/2} \tag{5}$$

where σ_0 is a friction stress; K_{HP} is a constant which reflects the boundary resistance to dislocation slip; and D_{av} is the grain size or boundary spacing [5]. In the case of pure Ni, $\sigma_0 = 20$MPa and $K_{HP} = 158\ \text{MPa}\cdot\mu m^{1/2}$ [37,66]. D_{av} is the only variable in the Hall–Petch equation, and it varies significantly for different types of zones in HS materials. In the soft zones of LNR-500 °C-13 min and ECAP+LNR-475 °C-5 min samples, in which the grains were equiaxed, values of D_{av} were measured to be 12.3 μm and 2.4 μm, respectively. In the hard zones of both LNR-500 °C-13 min and ECAP+LNR-475 °C-5 min samples, dislocation cells and grains are mostly elongated. Therefore, the equivalent boundary spacing of 0.32 μm and 0.26 μm was used in estimating the boundary strengthening effect in the LNR-500 °C-13 min and ECAP+LNR-475 °C-5 min samples, respectively (For readers' convenience, the D_{av} values for each type of zones are collected in Table 1). By substituting abovementioned parameters into Eq. (5), the strength increments due to boundary strengthening effect can be estimated for soft and hard zones in both LNR-500 °C-13 min and ECAP+LNR-475 °C-5 min samples, and are collected in Table 2.

The strength increment caused by strain hardening is usually expressed by the Bailey–Hirsch relationship [44,45]:

$$\sigma_\rho = M\alpha_T G b\sqrt{\rho_S + \rho_G} \tag{6}$$

where M is the dimensionless mean orientation factor, α_T is a temperature dependent constant, G is shear modulus, b is the Burgers vector, ρ_S is the density of SSDs and ρ_G is the density of GNDs. The values of α_T, G and b are normally taken to be 0.24, 79 GPa and 0.249 nm, respectively, for commercially pure Ni [67]. The mean orientation factor, M, depends on the texture and the orientation of the tensile axis at the meso-level [68,69], and also depends on the Schmid factor, local shear stress and the number of active slip systems at micro scale [69]. There are a few models available to estimate the M values for rolled fcc alloys with different textures, such as Taylor's model, Sachs model and Hutchinson's self-consistent model; Data are available in the work by Starink and Wang [69]. Since the volume fractions of detected textures in the LNR-500 °C-13 min and ECAP+LNR-475 °C-5 min samples have been extracted from Fig. 3, the volume weighted average M values for the LNR-500 °C-13 min and ECAP+LNR-475 °C-5 min samples have been estimated to be 3.2 and 3.1, respectively (note: the M values derived by Taylor's model have

Table 1
Microstructural variables measured from sample materials. (The subscripts "soft" and "hard" are used to identify soft and hard zones.)

Sample	$D_{av,soft}$ (μm)	$D_{av,hard}$ (μm)	$\rho_{total,soft}$ (m^{-2})	$\rho_{total,hard}$ (m^{-2})
LNR-500 °C-13min	12.3	0.32	5.7×10^{12}	8.4×10^{14}
ECAP+ LNR-475 °C-5min	2.4	0.26	4.5×10^{12}	7.0×10^{14}
LNR-500 °C-13 min (necking)	0.53 (cell size)	0.27	1.7×10^{14}	10.3×10^{14}
ECAP+ LNR-475 °C-5 min (necking)	0.51 (cell size)	0.20	0.94×10^{14}	9.1×10^{14}

been adopted for conservative estimation). Similar M values for the LNR-500 °C-13 min and ECAP+LNR-475 °C-5 min samples indicate that textures have little effect on discriminating the mechanical properties of the two HS materials.

Dislocation densities are the determinative variables in the Bailey–Hirsch equation. It is broadly accepted that the effects of SSDs and GNDs in strain hardening are equal. However, the physical characteristics of SSDs and GNDs are very different [47,68,70,71]. Theoretically speaking, each individual dislocation is a GND because it assures a local deformation with respect to its surroundings, in other words it is geometrically necessary. However, many dislocations with different Burgers vectors may lead to a collective strain of zero, and then they are recognized as SSDs. In practice, SSDs are those dislocations creating local misorientations less than 0.5 ° [48,68]. When counting SSDs and GNDs for strain hardening, there are several issues to consider. (1) Due to the effect of mutual attractions between SSDs of opposite signs, SSDs are quickly annihilated or recovered during heat treatments [70]; GNDs are less likely to be recovered, because they are necessary to accommodate strain gradients at boundaries; Thereby, GNDs govern the flow stress of heat-treated samples [47]. (2) The average slip distance of SSDs is significantly longer than that of GNDs; Therefore, at very high strains when grain refinement is reaching the ultrafine grained regime, the density of GNDs becomes significantly larger than that of SSDs ($\rho_G \gg \rho_s$) [67,70]. Accordingly, it is reasonable to assume that the flow stresses of the LNR-500 °C-13 min and ECAP+LNR-475 °C-5 min samples are governed by GNDs, and the densities of SSDs are approximately 10% of the total dislocation density [67,72]. This assumption is considered realistic for the ECAP+LNR-475 °C-5 min sample, in which the recrystallization textures are in dominance, the coarse grain sizes are below 10 μm and the ultrafine grain sizes are below 500 nm [47,70].

The densities of GNDs in soft and hard zones of the LNR-500 °C-13 min and ECAP+LNR-475 °C-5 min samples were calculated from EBSD data. Binning of 4 × 4 was used to provide an angular resolution in the range of 0.3 to 0.5 °, which is ideal for GND density measurement [73,74]. As suggested by the literature [75,76], the step size (spatial resolution) of EBSD analysis should be slightly smaller than the dislocation cell diameter to ensure a reasonable estimate of the dislocation density. If the step size is too large, the dislocation density will be underestimated, as undulations in the lattice curvature will be overlooked [75,76]. If the step size is too small, the uncertainty of the EBSD orientation determination will compound the error. In other words, if the step size is too small, the measured GND density will be mainly the noise of EBSD signal [75]. According to TEM analysis, the dislocation cell sizes of the undeformed soft zones, tensile-deformed soft zones and hard zones are in the ranges of 0.9 – 30 μm, 0.10 – 1.29 μm and 0.04 – 0.54 μm, respectively. Thus, the step sizes used for analyzing undeformed soft zones, tensile-deformed soft zones and hard zones are 1.5 μm, 0.2 μm and 0.05 μm, respectively.

The GND densities were calculated based on the strain gradient model by Gao et al. [77] and the equation provided by Kubin and Mortensen [70,73]:

$$\rho_{GND} = \frac{2\theta_{KAM}}{xb} \tag{7}$$

where x is unit length, which is equal to twice the step size used in EBSD acquisition [40,71]; b is the Burgers vector (b_{Ni} =0.249 nm); θ_{KAM} is the kernel average misorientation (KAM), which is retrieved directly from EBSD data. The KAM quantifies the average misorientation around each measurement point with respect to a defined set of nearest or nearest plus second-nearest neighbor points. KAM larger than 2° are excluded from the calculation, because these points are assumed to contribute to Hall–Petch strengthening [73,78].

Under the assumption that GNDs account for 90% of the total number of dislocations in each zone [67,72], the dislocation density in each type of the zones can be estimated by $\rho_{total} = \rho_s + \rho_G = \frac{\rho_G}{90\%}$, and the results are provided in Table 1.

For a homogeneous CG material, its yield strength can be estimated by the sum of Eqs. (5) and (6):

$$\sigma_y = \sigma_d + \sigma_\rho \tag{8}$$

However, the primary microstructural characteristic of single-phase HS materials is the large variation in grain sizes and/or dislocation structures as shown in Figs. 1 and 2. Thus, the strengths of the soft and hard zones have to be calculated separately and then substituted into the general rule of mixtures to estimate strength of the HS material. There have been many reports showing that the strength of HS materials may deviate noticeably from the estimation of the rule of mixtures. Such deviation has been attributed to the synergistic strengthening in the HS material [14,19]. Thus, an additional parameter, σ_{syn}, is introduced for HS materials. Then, the yield strength of a HS material can be expressed as:

$$\sigma_{y,HS} = f_{soft} \times \left(\sigma_{d,soft} + \sigma_{\rho,soft}\right) + f_{hard} \times \left(\sigma_{d,hard} + \sigma_{\rho,hard}\right) + \sigma_{syn} \tag{9}$$

where f_{soft} and f_{hard} are volume fractions of soft and hard zones in a HS material; The strength increments in soft and hard zones are calculated separately by Eqs. (5) and (6), and given in Table 2. The yield strength of the material is obtained by the tensile test, thus $\sigma_{y,HS}$ =

Table 2
Data for strength increments calculations. (The values of yield strength $\sigma_{y,test}$ and ultimate tensile strength $\sigma_{UTS,test}$ are obtained by tensile tests; The subscripts "*soft*" and "*hard*" are used to identify soft and hard zones.)

Sample	$\sigma_{UTS,test}$ (MPa)	$\sigma_{y,test}$ (MPa)	$\sigma_{d,soft}$ (MPa)	$\sigma_{\rho,soft}$ (MPa)	$\sigma_{d,hard}$ (MPa)	$\sigma_{\rho,hard}$ (MPa)	σ_{syn} (MPa)
LNR-500 °C-13min		467.4	65.1	36.1	299.3	436.7	1.2
ECAP+ LNR-475 °C-5min		577.5	122.0	31.0	329.9	387.2	168.4
LNR-500 °C-13 min (necking)	624.7		237.0	195.0	325.2	485.6	−25.2
ECAP+ LNR-475 °C-5 min (necking)	694.8		241.2	142.2	373.3	441.8	115.4

$\sigma_{y,test}$ and is provided in Table 2. Thereby, the strength increments due to synergistic strengthening in LNR-500 °C-13 min and ECAP +LNR-475 °C-5 min samples are found to be 1.2 MPa and 168.4 MPa, respectively. The synergistic strengthening is clearly strong in the ECAP+LNR-475 °C-5 min sample, but seemingly negligible in the LNR-500 °C-13 min sample. Since both LNR-500 °C-13 min and ECAP +LNR-475 °C-5 min samples are HS single-phase materials, the synergistic strengthening effect is solely due to the microstructural heterogeneities. Thus, the synergistic strengthening effect in the current case is equivalent to the HDI strengthening effect.

5. Discussions

5.1. Grain size, dislocations and slip bands

As shown in Fig. 10c, slip bands are all over the surface of the LNR-500 °C-13 min sample at necking, although the densities of the slip bands seem to vary from grain to grain. This indicates that dislocation slip is the major deformation mechanism in both hard and soft zones of the LNR-500 °C-13 min sample. In contrast, slip bands are only observed in the deformed soft zones in the ECAP+LNR-475 °C-5 min sample as shown in Fig. 11c. In the dislocation slip dominated deformation process, many dislocations may assemble on a set of parallel and adjacent slip planes; These dislocation loops eventually will reach the sample surface to form a visible slip band as the plastic deformation proceeds [49]. Once a slip band forms, it becomes a plastic deformation highway on which dislocations can cross-slip, multiply and move at high velocities. As a result, plastic deformation is accommodated by high rates of dislocation generation and slip within the slip bands, and the number of slip bands increases with the stress and strain [63]. As the grain size decreases, the critical resolved shear stress (CRSS) for dislocation slip increases [5] and GB mediated mechanisms become active [9], thereby the chance for dislocations to assemble into a slip band is reduced. Consequently, slip bands are less likely to be visible in the ultrafine grains of the ECAP +LNR-475 °C-5 min sample.

Analysis based on EBSD data reveals that the dislocation densities in the soft and hard zones of the LNR-500 °C-13 min sample are 1.7×10^{14} m^{-2} and 10.3×10^{14} m^{-2}, respectively, at the onset of necking. These values are higher than the dislocation densities of 0.94×10^{14} m^{-2} and 9.1×10^{14} m^{-2} in the soft and hard zones of the ECAP+LNR-475 °C-5 min sample at the onset of necking, respectively. The average cell sizes and grain sizes in the HS Ni samples, at the onset of necking, are also provided in Table 1. By substituting the grain sizes and dislocation densities into Eqs. (5) and (6), respectively, the strength increments due to Hall-Petch strengthening and strain hardening at the onset of necking can be estimated, and are given in Table 2. If the synergistic strengthening effects are ignored, the volume weighted flow stresses at the onset of necking of the LNR-500 °C-13 min and ECAP+LNR-475 °C-5 min samples are estimated to be 649.9 MPa and 579.4 MPa, respectively. Interestingly, the estimated flow stress in the LNR-500 °C-13 min sample are higher than that of the ECAP+LNR-475 °C-5 min sample at necking, although the average grain size in the LNR-500 °C-13 min sample is larger. This is because the dislocation density in the LNR-500 °C-13 min sample is significantly higher than that in the ECAP+LNR-475 °C-5 min sample at necking, and the Hall-Petch strengthening in the LNR-500 °C-13 min sample is over estimated.

If now the synergistic strengthening due to heterostructure is taken into account, the flow stress at necking shall theoretically equal to the UTS of the material. The UTS of the LNR-500 °C-13 min and ECAP+LNR-475 °C-5 min samples are 624.7 MPa and 694.8 MPa, respectively. The strength increments due to the synergistic strengthening are calculated to be −25.2 MPa and 115.4 MPa in the LNR-500 °C-13 min and ECAP+LNR-475 °C-5 min samples, respectively. Provided that the uniform elongations of both materials are very close as shown in Fig. 12a, the synergistic strengthening due to the grouping of ultrafine grains and coarse grains in the ECAP+LNR-475 °C-5 min sample is evidently stronger. The heterostructure possessed by the LNR-500 °C-13 min sample seems unbeneficial for the mechanical property optimization.

It should be noted that both Bailey–Hirsch relationship and Hall-Petch relationship are empirical. The results estimated by both relationships are influenced by the choice of the constants and the experimentally measured variables. For instance, when estimating the strength of the hard zone in the LNR-500 °C-13 min sample, a portion of extended dislocation boundaries are recognized as GBs although they are non-equilibrium boundaries and thus offer much less resistance to dislocation slip than well-developed GBs. Hence, the strength of the hard zone in the LNR-500 °C-13 min sample has been overestimated, leading to small and even negative synergistic strengthening increments. However, as shown in Fig. 12d the HDI stress in the LNR-500 °C-13 min sample is significantly stronger than the CG sample, indicating that the strong HDI stress is also available to cause the synergistic strengthening. To sum up, by combining empirical estimation and experimental measurement the superior synergistic strengthening effect in the ECAP+LNR-475 °C-5 min sample is clearly identified; High densities of dislocations and high HDI stresses in both deformed LNR-500 °C-13 min and ECAP+LNR-475 °C-5 min samples have led to a conclusion that synergistic strengthening effect is present in both materials with heterostructures.

5.2. Interfaces

Interfaces play a critical role in determining the mechanical properties of a polycrystalline material. In a HS single-phase material, there are two types of interfaces: (1) GBs and (2) zone boundaries. GBs offer resistance to dislocation slip, because an energy of reaction (high stress) is required for a dislocation to change its core structure and slip system while transmitting through the GB [79]. A zone boundary offers stronger resistance to dislocation slip than a GB [80], due to the sharp change in grain sizes from the soft zone to the hard zone. As a result, an extensive amount of dislocations will accumulate along zone boundaries as plastic deformation proceeds, and build up strong strain gradients and stress gradients [13,22]. In this sense, the zone boundaries in HS single-phase materials are similar to the phase boundaries in dual phase materials [5,81]. In the LNR-500 °C-13 min sample, dislocations have accumulated on and evenly distributed along the zone boundary with a high density on the hard zone side and a low density on the soft zone side, as shown in Fig. 4b. In the ECAP+LNR-475 °C-5 min sample, dislocations are also found along the zone boundaries. In addition, on the hard zone side, there are numerous closely spaced triple junctions as shown in Fig. 5b, Fig. S2c and d. These triple junctions are believed effective in distributing stress concentrations [82], and thus to reduce the chance of crack nucleation, as evidenced by the absence of crack in the TEM samples of the ECAP+LNR-475 °C-5 min sample. These triple junctions as a part of the zone boundaries are also effective in delaying crack propagation by frequently changing crack directions [83]. Although the cracks found in Figs. 6 and 8 are not created during the tensile test, they are evidences of high stress concentration and strong tendency for stress relief. Under three-dimensional constraint, crack initiation is delayed within the bulk material. As dislocations continue to accumulate along zone boundaries, the boundaries tilt gradually to reduce the angle between the boundaries and the global applied stress. As a result, the resolved shear stresses parallel to the zone boundaries increase, leading to intensified dislocation slip parallel to the interface. From the perspective of dislocation mechanics, intensified dislocation accumulation in a local area will eventually collapse (for stress relief) in the form of shear band and/or crack [5,52].

5.3. Shear bands

At the onset of necking, the strengths of the soft and hard zones of the LNR-500 °C-13 min sample are estimated by Eq. (8) to be 432.0 MPa and 810.8 MPa, respectively. In the ECAP+LNR-475 °C-5 min sample, the strengths of the soft and hard zones are estimated to be 383.4 MPa and 815.1 MPa, respectively. The results demonstrate that the strength differences between soft and hard zones are still large, even when the UTS is reached in the HS Ni samples. The strength difference between soft and hard zones leads to microscopic strain and stress partitioning behaviors. During plastic deformation, hard zone is subjected to a much higher stress than soft zone, but meanwhile the plastic strain in the hard zone is much lower [15,81,84]. As a result, stress gradient and strain gradient increase at the zone boundary area, leading to the high HDI stress [15]. HDI stress consists of a forward-stress and a back-stress. The stresses act in opposite directions and tend to balance each other at the zone boundary. Forward-stress adds to the applied stress in the hard zone to promote its deformation [15]. While the strain hardening rate in the hard zone is still limited, shear banding may become active as a form of plastic instability [54], as evidenced in Figs. 10 and 11.

For the LNR-500 °C-13 min sample, shear bands are very likely to initiate in the hard zone that contains an extremely high density of dislocations. High density of dislocations will slow down dislocation generation and lower strain hardening rate. Once a shear band initiates in the hard zone, preexisting dislocation structures quickly collapse in the dislocation avalanche and are consumed by the growing shear band. The major deformation mechanisms in both the soft and hard zones are dislocation slip, and the grain sizes in both zones are similar; with only a few shear bands to accommodate strain localization, the shear bands can quickly expand across both soft and hard zones, leading to catastrophic failure of the material as shown in Figs. 10 and 12a.

Micro-shear-bands have been frequently observed in the hard zones of the ECAP+LNR-475 °C-5 min sample, at the onset of necking, as described in Section 3.2. The shear strain associated with each micro-shear-band is in the range of $0.94 - 2.65$ (the method used for estimating the shear strain is described elsewhere [85]). The density of the micro-shear-band is as high as 2.21×10^9 m^{-2} in the region of necking. Therefore, micro-shear-bands clearly play an important role in strain accommodation in the hard zone. For fcc metals, the strain rate sensitivity increases with the decreasing grain size [5,86]. Hence, ultrafine-grained materials exhibit a noticeably higher strain rate sensitivity of the flow stress than their CG counterparts, and this is supposed to increase the resistance of ultrafine-grained materials against shear banding [86]. However, micro-shear-bands have been observed in ultrafine-grained fcc materials at very low strain rates ($<10^{-4}$ s^{-1}), and the grain boundary sliding mechanism has also been noticed in conjunction with micro shear banding [9]. This is because the low strain rate lowers strain-hardening rate [52] and provides sufficient time for grain boundary sliding towards shear stress concentration [9]. In the case of HS materials such as the ECAP+LNR-475 °C-5 min sample, the shear strain gradient at the zone boundary requires additional strain accommodation while strain hardening is retarded by small grain size. Thus, grain boundary sliding is promoted in conjunction with micro shear banding for localized strain accommodation in the hard zone at a global strain rate of 1.6×10^{-3} s^{-1}. Once a shear band initiates at a zone boundary due to high local strain concentration, it quickly expands in the hard zone to reach another zone boundary. However, transmission of the shear band towards soft zone is delayed at zone boundary, because pronounced dislocation emission or slip transfer will occur in the coarse grain to reduce the magnitude of the local stress concentration. In other words, the high resistance of the soft zones to shear banding is attained by the high strain-hardening capability. This is evidenced by the appearance of intense slip bands at the tips of the shear band as shown in Fig. 11c (the red arrow on the top is intentionally shifted to the right to avoid overlapping with the bundle of intense slip bands).

When the plastic strain is sufficiently high, local stress concentrations may be too high to be accommodated by dislocation slip, and then shear bands will expand into soft zones. Eventually, numerous micro-shear-bands intercross one another to form net-like structure as shown in Fig. 11a and b, and continuous agglomeration of shear bands leads to failure of the material. There are recently a few reports on the delocalization of shear bands in HS materials [22,43,50,51]. In these reports, shear bands were detected by digital image correlation (DIC) analysis of local strains rather than actual observation of shear band structures, and shear bands were detected at low strain level during uniform elongation. Moreover, the sizes of the shear bands reported in literatures are similar to the ones found in current study [22,43]. However, to date structural shear bands as a form of plastic instability have only been observed in necking region of tensile samples [9]. Therefore, the shear bands detected by DIC technique in uniform elongation region of the sample are supposedly precursors of micro-shear-bands [22,50]. Nevertheless, the early work of DIC strain analysis of HS materials reveals that high strain concentrations are at zone boundaries [22,50], which supports the hypothesis of shear banding initiation at zone boundaries.

6. Conclusions

Two distinct types of heterostructures were introduced to pure Ni samples. Critical microstructures and defects in HS Ni samples and their effects on mechanical properties were systematically studied. Based on detailed experimental work and calculations, several conclusions can be drawn as follows

1) High densities of dislocations and high HDI stresses were developed during the tensile tests of the LNR-500 °C-13 min and ECAP+LNR-475 °C-5 min samples, due to the microstructural heterogeneity. The YS and UTS of both HS Ni samples are better than those predicted by the rule of mixtures, indicating the synergistic strengthening effects in both types of heterostructures. The outstanding synergistic strengthening effect in the ECAP+LNR-475 °C-5 min sample is attributed to the combination of CG zones and ultrafine-grained matrix.
2) In the architecture of CG zones in ultrafine-grained matrix, numerous triple junctions are attached to the interfaces between CG zones and ultrafine-grained matrix. The triple junctions effectively reduce the magnitudes of local stress concentrations; Thus, crack initiation is delayed in the HS material. Meanwhile, triple junctions also act as obstacles to crack propagation. Consequently, the ECAP+LNR-475 °C-5 min sample having the CG zones embedded in the ultrafine-grained matrix is less prone to crack than the LNR-500 °C-13 min sample.
3) Net-like patterns formed by the intercrossing micro-shear-bands have been observed on the surface of tensile-deformed ECAP+LNR-475 °C-5 min samples, but not on the tensile-deformed LNR-500 °C-13 min samples. This is because micro-shear-bands can only form in well-developed ultrafine-grained structures, in which the shear strain gradients at the zone boundaries require additional strain accommodations while strain hardening is retarded by small grain sizes. Net-like distribution of micro-shear-bands is a result of the shear band delocalization in the HS material. The current experimental result suggests that the shear band delocalization and dispersion can only be realized in the heterostructure containing a mixture of CG zones and ultrafine-grained/nano-crystalline zones.

Declaration of Competing Interest

The authors declare that they have no known competing financial interests or personal relationships that could have appeared to influence the work reported in this paper

Acknowledgments

This work is supported by the National Key R&D Program of China (2017YFA0204403) ,National Natural Science Foundation of China (51931003 (Y.T.Z), 51601094 (Y.C.) and 51601003 (H.Z.)), the Fundamental Research Funds for the Central Universities (30918011342) and the China Scholarship Council (201906840083). The authors are thankful for the technical support from Jiangsu Key Laboratory of Advanced Micro&Nano Materials and Technology, and the Materials Characterization Facility of Nanjing University of Science and Technology.

Supplementary materials

Supplementary material associated with this article can be found in the online version at doi:10.1016/j.actamat.2020.03.001.

References

[1] X. Li, K. Lu, Playing with defects in metals, Nat. Mater. 16 (7) (2017) 700–701.
[2] S.H. Jiang, H. Wang, Y. Wu, X.J. Liu, H.H. Chen, M.J. Yao, B. Gault, D. Ponge, D. Raabe, A. Hirata, M.W. Chen, Y.D. Wang, Z.P. Lu, Ultrastrong steel via minimal lattice misfit and high-density nanoprecipitation, Nature 544 (7651) (2017) 460–464.
[3] Y.T. Zhu, X.Z. Liao, Nanostructured metals - Retaining ductility, Nat. Mater. 3 (6) (2004) 351–352.
[4] Y. Estrin, A. Vinogradov, Extreme grain refinement by severe plastic deformation: a wealth of challenging science, Acta Mater. 61 (3) (2013) 782–817.
[5] Y. Cao, S. Ni, X.Z. Liao, M. Song, Y.T. Zhu, Structural evolutions of metallic materials processed by severe plastic deformation, Mater. Sci. Eng. R: Rep. 133 (2018) 1–59.
[6] M.Y. Gutkin, I.A. Ovid'ko, N.V. Skiba, Crossover from grain boundary sliding to rotational deformation in nanocrystalline materials, Acta Mater. 51 (14) (2003) 4059–4071.
[7] Q. Wei, L. Kecskes, T. Jiao, K.T. Hartwig, K.T. Ramesh, E. Ma, Adiabatic shear banding in ultrafine-grained Fe processed by severe plastic deformation, Acta Mater. 52 (7) (2004) 1859–1869.
[8] Y.B. Wang, B.Q. Li, M.L. Sui, S.X. Mao, Deformation-induced grain rotation and growth in nanocrystalline Ni, Appl. Phys. Lett. 92 (1) (2008) 011903.
[9] I. Sabirov, Y. Estrin, M.R. Barnett, I. Timokhina, P.D. Hodgson, Tensile deformation of an ultrafine-grained aluminium alloy: micro shear banding and grain boundary sliding, Acta Mater. 56 (10) (2008) 2223–2230.
[10] I.A. Ovid'ko, R.Z. Valiev, Y.T. Zhu, Review on superior strength and enhanced ductility of metallic nanomaterials, Prog. Mater. Sci. 94 (2018) 462–540.
[11] Y.M. Wang, E. Ma, Three strategies to achieve uniform tensile deformation in a nanostructured metal, Acta Mater. 52 (6) (2004) 1699–1709.
[12] X.L. Wu, M.X. Yang, F.P. Yuan, G.L. Wu, Y.J. Wei, X.X. Huang, Y.T. Zhu, Heterogeneous lamella structure unites ultrafine-grain strength with coarse-grain ductility, PNAS 112 (47) (2015) 14501–14505.
[13] X.L. Wu, Y.T. Zhu, Heterogeneous materials: a new class of materials with unprecedented mechanical properties, Mater. Res. Lett. 5 (8) (2017) 527–532.
[14] E. Ma, T. Zhu, Towards strength–ductility synergy through the design of heterogeneous nanostructures in metals, Mater. Today 20 (6) (2017) 323–331.
[15] Y.T. Zhu, X.L. Wu, Perspective on hetero-deformation induced (HDI) hardening and back stress, Mater. Res. Lett. 7 (10) (2019) 393–398.
[16] K. Lu, Making strong nanomaterials ductile with gradients, Science 345 (6203) (2014) 1455–1456.
[17] X.L. Wu, P. Jiang, L. Chen, F.P. Yuan, Y.T. Zhu, Extraordinary strain hardening by gradient structure, Proc. Natl. Acad. Sci. 111 (20) (2014) 7197–7201.
[18] T.H. Fang, W.L. Li, N.R. Tao, K. Lu, Revealing extraordinary intrinsic tensile plasticity in gradient nano-grained copper, Science 331 (6024) (2011) 1587–1590.
[19] X.L. Wu, P. Jiang, L. Chen, J.F. Zhang, F.P. Yuan, Y.T. Zhu, Synergetic strengthening by gradient structure, Mater. Res. Lett. 2 (4) (2014) 185–191.
[20] Y.J. Wei, Y.Q. Li, L.C. Zhu, Y. Liu, X.Q. Lei, G. Wang, Y.X. Wu, Z.L. Mi, J.B. Liu, H.T. Wang, H.J. Gao, Evading the strength–ductility trade-off dilemma in steel through gradient hierarchical nanotwins, Nat. Commun. 5 (2014) 3580.
[21] Z. Cheng, H.F. Zhou, Q.H. Lu, H.J. Gao, L. Lu, Extra strengthening and work hardening in gradient nanotwinned metals, Science 362 (6414) (2018) 1–8 eaau1925.
[22] C.X. Huang, Y.F. Wang, X.L. Ma, S. Yin, H.W. Höppel, M. Göken, X.L. Wu, H.J. Gao, Y.T. Zhu, Interface affected zone for optimal strength and ductility in heterogeneous laminate, Mater. Today 21 (7) (2018) 713–719.
[23] X.L. Ma, C.X. Huang, J. Moering, M. Ruppert, H.W. Höppel, M. Göken, J. Narayan, Y.T. Zhu, Mechanical properties of copper/bronze laminates: Role of interfaces, Acta Mater. 116 (2016) 43–52.
[24] T. Nizolek, I.J. Beyerlein, N.A. Mara, J.T. Avallone, T.M. Pollock, Tensile behavior and flow stress anisotropy of accumulative roll bonded Cu-Nb nanolaminates, Appl. Phys. Lett. 108 (5) (2016) 051903.
[25] J. Wang, I.J. Beyerlein, N.A. Mara, D. Bhattacharyya, Interface-facilitated deformation twinning in copper within submicron ag-cu multilayered composites, Scr. Mater. 64 (12) (2011) 1083–1086.
[26] S.J. Zheng, J. Wang, J.S. Carpenter, W.M. Mook, P.O. Dickerson, N.A. Mara, I.J. Beyerlein, Plastic instability mechanisms in bimetallic nanolayered composites, Acta Mater. 79 (2014) 282–291.
[27] H.W. Yen, S.W. Ooi, M. Eizadjou, A. Breen, C.-Y. Huang, H.K.D.H. Bhadeshia, S.P. Ringer, Role of stress-assisted martensite in the design of strong ultrafine-grained duplex steels, Acta Mater. 82 (2015) 100–114.
[28] Y. Cao, Y.B. Wang, X.H. An, X.Z. Liao, M. Kawasaki, S.P. Ringer, T.G. Langdon, Y.T. Zhu, Concurrent microstructural evolution of ferrite and austenite in a duplex stainless steel processed by high-pressure torsion, Acta Mater. 63 (2014) 16–29.
[29] X.H. An, S.M. Zhu, Y. Cao, M. Kawasaki, X.Z. Liao, S.P. Ringer, J.F. Nie, T.G. Langdon, Y.T. Zhu, Atomic-scale investigation of interface-facilitated deformation twinning in severely deformed Ag-Cu nanolamellar composites, Appl. Phys. Lett. 107 (1) (2015) 011901.
[30] C. Sawangrat, S. Kato, D. Orlov, K. Ameyama, Harmonic-structured copper, performance and proof of fabrication concept based on severe plastic deformation of powders, J. Mater. Sci. 49 (19) (2014) 6579–6585.
[31] Z. Zhang, S.K. Vajpai, D. Orlov, K. Ameyama, Improvement of mechanical properties in SUS304L steel through the control of bimodal microstructure characteristics, Mater. Sci. Eng. A 598 (2014) 106–113.
[32] S.K. Vajpai, M. Ota, T. Watanabe, R. Maeda, T. Sekiguchi, T. Kusaka, K. Ameyama, The development of high performance Ti-6Al-4V alloy via a unique microstructural design with bimodal grain size distribution, Metall. Mater. Trans. A 46 (2) (2015) 903–914.
[33] Y.M. Wang, M.W. Chen, F.H. Zhou, E. Ma, High tensile ductility in a nanostructured metal, Nature 419 (6910) (2002) 912–915.
[34] B.Q. Han, J.Y. Huang, Y.T. Zhu, E.J. Lavernia, Strain rate dependence of properties of cryomilled bimodal 5083 al alloys, Acta Mater. 54 (11) (2006) 3015–3024.
[35] Y. Zhao, T. Topping, J.F. Bingert, J.J. Thornton, A.M. Dangelewicz, Y. Li, W. Liu, Y. Zhu, Y. Zhou, E.J. Lavernia, High tensile ductility and strength in bulk nanostructured nickel, Adv. Mater. 20 (16) (2008) 3028–3033.
[36] B.Q. Han, Z. Lee, D. Witkin, S. Nutt, E.J. Lavernia, Deformation behavior of bimodal nanostructured 5083 al alloys, Metall. Mater. Trans. A Phys. Metall. Mater. Sci. 36A (4) (2005) 957–965.
[37] T.R. Lee, C.P. Chang, P.W. Kao, The tensile behavior and deformation microstructure of cryo-rolled and annealed pure nickel, Mater. Sci. Eng. A 408 (1–2) (2005) 131–135.
[38] J.S. Moya, S. Lopez-Esteban, C. Pecharromán, The challenge of ceramic/metal microcomposites and nanocomposites, Prog. Mater. Sci. 52 (7) (2007) 1017–1090.
[39] I. Sabirov, O. Kolednik, R.Z. Valiev, R. Pippan, Equal channel angular pressing of metal matrix composites: Effect on particle distribution and fracture toughness, Acta Mater. 53 (18) (2005) 4919–4930.
[40] Y.F. Liu, F. Wang, Y. Cao, J.F. Nie, H. Zhou, H.B. Yang, X.F. Liu, X.H. An, X.Z. Liao, Y.H. Zhao, Y.T. Zhu, Unique defect evolution during the plastic deformation of a metal matrix composite, Scr. Mater. 162 (2019) 316–320.
[41] L.J. Huang, L. Geng, H.X. Peng, Microstructurally inhomogeneous composites: Is a homogeneous reinforcement distribution optimal? Prog. Mater. Sci. 71 (2015) 93–168.
[42] N. Jia, Z.H. Cong, X. Sun, S. Cheng, Z.H. Nie, Y. Ren, P.K. Liaw, Y.D. Wang, An in situ high-energy X-ray diffraction study of micromechanical behavior of multiple phases in advanced high-strength steels, Acta Mater. 57 (13) (2009) 3965–3977.
[43] F.P. Yuan, D.S. Yan, J.D. Sun, L.L. Zhou, Y.T. Zhu, X.L. Wu, Ductility by shear band delocalization in the nano-layer of gradient structure, Mater. Res. Lett. 7 (1) (2019) 12–17.
[44] J.E. Bailey, P.B. Hirsch, The dislocation distribution, flow stress, and stored energy in cold-worked polycrystalline silver, Philos. Mag. A J. Theor. Exp. Appl. Phys. 5 (53) (1960) 485–497.
[45] U.F. Kocks, H. Mecking, Physics and phenomenology of strain hardening: the FCC case, Prog. Mater. Sci. 48 (3) (2003) 171–273.
[46] D. Kuhlmann-Wilsdorf, High-strain dislocation patterning, texture formation and shear banding of wavy glide materials in the LEDS theory, Scr. Mater. 36 (2) (1997) 173–181.
[47] C. Zhu, T. Harrington, G.T. Gray, K.S. Vecchio, Dislocation-type evolution in quasi-statically compressed polycrystalline nickel, Acta Mater. 155 (2018) 104–116.
[48] B. Bay, N. Hansen, D.A. Hughes, D. Kuhlmann-Wilsdorf, Overview no. 96 evolution of FCC deformation structures in polyslip, Acta Metall. Mater. 40 (2) (1992) 205–219.
[49] T. Benjamin Britton, A.J. Wilkinson, Stress fields and geometrically necessary dislocation density distributions near the head of a blocked slip band, Acta Mater. 60 (16) (2012) 5773–5782.
[50] Y.F. Wang, C.X. Huang, Q. He, F.J. Guo, M.S. Wang, L.Y. Song, Y.T. Zhu, Heterostructure induced dispersive shear bands in heterostructured Cu, Scr. Mater. 170 (2019) 76–80.
[51] Y.F. Wang, C.X. Huang, Y.S. Li, F.J. Guo, Q. He, M.S. Wang, X.L. Wu, R.O. Scattergood, Y. Zhu, Dense dispersed shear bands in gradient-structured Ni, Int. J. Plast. 124 (2019) 186–198.
[52] R.W. Armstrong, F.J. Zerilli, Dislocation mechanics aspects of plastic instability and shear banding, Mech. Mater. 17 (2) (1994) 319–327.

[53] J.G. Li, Y.L. Li, C.X. Huang, T. Suo, Q.M. Wei, On adiabatic shear localization in nanostructured face-centered cubic alloys with different stacking fault energies, Acta Mater. 141 (2017) 163–182.
[54] I.S. Yasnikov, Y. Estrin, A. Vinogradov, What governs ductility of ultrafine-grained metals? A microstructure based approach to necking instability, Acta Mater. 141 (2017) 18–28.
[55] S.D. Antolovich, R.W. Armstrong, Plastic strain localization in metals: origins and consequences, Prog. Mater. Sci. 59 (2014) 1–160.
[56] F. Liu, H. Yuan, S. Goel, Y. Liu, J.T. Wang, Bulk nanolaminated nickel: Preparation, microstructure, mechanical property, and thermal stability, Metall. Mater. Trans. A 49 (2) (2018) 576–594.
[57] R.Z. Valiev, T.G. Langdon, Principles of equal-channel angular pressing as a processing tool for grain refinement, Prog. Mater. Sci. 51 (7) (2006) 881–981.
[58] S.B. Lee, D.Y. Yoon, N.M. Hwang, M.F. Henry, Grain boundary faceting and abnormal grain growth in nickel, Metall. Mater. Trans. A 31 (3) (2000) 985–994.
[59] P.W. Trimby, Y. Cao, Z. Chen, S. Han, K.J. Hemker, J. Lian, X. Liao, P. Rottmann, S. Samudrala, J. Sun, J.T. Wang, J. Wheeler, J.M. Cairney, Characterizing deformed ultrafine-grained and nanocrystalline materials using transmission Kikuchi diffraction in a scanning electron microscope, Acta Mater. 62 (0) (2014) 69–80.
[60] H.W. Zhang, X. Huang, N. Hansen, Evolution of microstructural parameters and flow stresses toward limits in nickel deformed to ultra-high strains, Acta Mater. 56 (19) (2008) 5451–5465.
[61] E.A. Holm, D.L. Olmsted, S.M. Foiles, Comparing grain boundary energies in face-centered cubic metals: Al, Au, Cu and Ni, Scr. Mater. 63 (9) (2010) 905–908.
[62] D.E. Kramer, M.F. Savage, L.E. Levine, AFM observations of slip band development in Al single crystals, Acta Mater. 53 (17) (2005) 4655–4664.
[63] Z.Q. Wang, I.J. Beyerlein, R. LeSar, Slip band formation and mobile dislocation density generation in high rate deformation of single FCC crystals, Philos. Mag. 88 (9) (2008) 1321–1343.
[64] M.X. Yang, Y. Pan, F.P. Yuan, Y.T. Zhu, X.L. Wu, Back stress strengthening and strain hardening in gradient structure, Mater. Res. Lett. 4 (3) (2016) 145–151.
[65] H. Wang, Z.S. You, L. Lu, Kinematic and isotropic strain hardening in copper with highly aligned nanoscale twins, Mater. Res. Lett. 6 (6) (2018) 333–338.
[66] N. Hansen, Hall–Petch relation and boundary strengthening, Scr. Mater. 51 (8) (2004) 801–806.
[67] D.A. Hughes, N. Hansen, Microstructure and strength of nickel at large strains, Acta Mater. 48 (11) (2000) 2985–3004.
[68] L.S. Toth, C.F. Gu, B. Beausir, J.J. Fundenberger, M. Hoffman, Geometrically necessary dislocations favor the Taylor uniform deformation mode in ultra-fine-grained polycrystals, Acta Mater. 117 (2016) 35–42.
[69] M.J. Starink, S.C. Wang, A model for the yield strength of overaged Al–Zn–Mg–Cu alloys, Acta Mater. 51 (17) (2003) 5131–5150.
[70] L.P. Kubin, A. Mortensen, Geometrically necessary dislocations and strain-gradient plasticity: a few critical issues, Scr. Mater. 48 (2) (2003) 119–125.
[71] P.J. Konijnenberg, S. Zaefferer, D. Raabe, Assessment of geometrically necessary dislocation levels derived by 3D EBSD, Acta Mater. 99 (2015) 402–414.
[72] J. Pešička, R. Kužel, A. Dronhofer, G. Eggeler, The evolution of dislocation density during heat treatment and creep of tempered martensite ferritic steels, Acta Mater. 51 (16) (2003) 4847–4862.
[73] M. Calcagnotto, D. Ponge, E. Demir, D. Raabe, Orientation gradients and geometrically necessary dislocations in ultrafine grained dual-phase steels studied by 2D and 3D EBSD, Mater. Sci. Eng. A 527 (10) (2010) 2738–2746.
[74] P. Bate, R. Knutsen, I. Brough, F. Humphreys, The characterization of low–angle boundaries by EBSD, J. Microsc. 220 (1) (2005) 36–46.
[75] J. Jiang, T. Britton, A. Wilkinson, Measurement of geometrically necessary dislocation density with high resolution electron backscatter diffraction: effects of detector binning and step size, Ultramicroscopy 125 (2013) 1–9.
[76] D. Field, C. Merriman, N. Allain-Bonasso, F. Wagner, Quantification of dislocation structure heterogeneity in deformed polycrystals by EBSD, Model. Simul. Mater. Sci. Eng. 20 (2) (2012) 024007.
[77] H. Gao, Y. Huang, W. Nix, J. Hutchinson, Mechanism-based strain gradient plasticity—I. Theory, J. Mech. Phys. Solids 47 (6) (1999) 1239–1263.
[78] N. Hansen, Boundary strengthening in undeformed and deformed polycrystals, Mater. Sci. Eng. A 409 (1-2) (2005) 39–45.
[79] W.S. Yu, Z.Q. Wang, Interactions between edge lattice dislocations and $\Sigma 11$ symmetrical tilt grain boundaries in copper: a quasi-continuum method study, Acta Mater. 60 (13) (2012) 5010–5021.
[80] S. Lefebvre, B. Devincre, T. Hoc, Yield stress strengthening in ultrafine-grained metals: A two-dimensional simulation of dislocation dynamics, J. Mech. Phys. Solids 55 (4) (2007) 788–802.
[81] C.C. Tasan, M. Diehl, D. Yan, C. Zambaldi, P. Shanthraj, F. Roters, D. Raabe, Integrated experimental–simulation analysis of stress and strain partitioning in multiphase alloys, Acta Mater. 81 (2014) 386–400.
[82] C.R. Chen, S.X. Li, Distribution of stresses and elastic strain energy in an ideal multicrystal model, Mater. Sci. Eng. A 257 (2) (1998) 312–321.
[83] A. Pineau, A.A. Benzerga, T. Pardoen, Failure of metals I: Brittle and ductile fracture, Acta Mater. 107 (2016) 424–483.
[84] Z.H. Cong, N. Jia, X. Sun, Y. Ren, J. Almer, Y.D. Wang, Stress and strain partitioning of ferrite and martensite during deformation, Metall. Mater. Trans. A 40 (6) (2009) 1383–1387.
[85] C.S. Hong, N.R. Tao, X. Huang, K. Lu, Nucleation and thickening of shear bands in nano-scale twin/matrix lamellae of a Cu–Al alloy processed by dynamic plastic deformation, Acta Mater. 58 (8) (2010) 3103–3116.
[86] Y.Z. Guo, Y.L. Li, Z. Pan, F.H. Zhou, Q. Wei, A numerical study of microstructure effect on adiabatic shear instability: application to nanostructured/ultrafine grained materials, Mech. Mater. 42 (11) (2010) 1020–1029.